GaN/AlGaN-BASED UV PHOTODETECTORS WITH PERFORMANCES EXCEEDING THE PMTS

A DISSERTATION
SUBMITTED TO THE DEPARTMENT OF PHYSICS
AND THE INSTITUTE OF ENGINEERING AND SCIENCES
OF BILKENT UNIVERSITY
IN PARTIAL FULLFILMENT OF THE REQUIREMENTS
FOR THE DEGREE OF
DOCTOR OF PHILOSOPHY

By
Turgut Tut
September 2008

I certify that I have read this thesis and that in my opinion it is fully adequate, in scope and in quality, as a dissertation for the degree of Doctor of Philosophy.

Prof. Dr. Ekmel Özbay (Supervisor)

I certify that I have read this thesis and that in my opinion it is fully adequate, in scope and in quality, as a dissertation for the degree of Doctor of Philosophy

Assist. Prof. Hilmi Volkan Demir (E.E.E.)

I certify that I have read this thesis and that in my opinion it is fully adequate, in scope and in quality, as a dissertation for the degree of Doctor of Philosophy.

Assist. Prof. Ceyhun Bulutay

I certify that I have read this thesis and that in my opinion it is fully adequate, in scope and in quality, as a dissertation for the degree of Doctor of Philosophy.

Assoc. Prof. Oğuz Gülseren

I certify that I have read this thesis and that in my opinion it is fully adequate, in scope and in quality, as a dissertation for the degree of Doctor of Philosophy

Prof. Dr. Süleyman Özçelik

Approved for the Institute of Engineering and Sciences:

Prof. Mehmet B. Baray
Director of Institute of Engineering and Sciences

ABSTRACT

GaN/AlGaN-BASED UV PHOTODETECTORS WITH PERFORMANCES EXCEEDING THE PMTS

Turgut Tut
Ph.D. in Physics
Supervisor: Prof. Dr. Ekmel Ozbay

Sepptember 2008

The recent developments in high Al-content Al*x*Ga1−*x*N material growth technology made it possible to fabricate high performance solar-blind photodetectors operating in the ultraviolet (UV) spectral region with improved receiver sensitivity, low noise, low dark current density, and high speed. AlGaN-based Schottky, *p*-*i*-*n*, and metal-semiconductor-metal photodetectors (MSM) with very high performances have already been demonstrated. The UV-filtering nature of the atmospheric ozone molecules blocks the solar radiation to reach the earth's surface for wavelengths shorter than 280 nm. In this case, UV photodetectors with cutoff wavelengths around 280 nm, which are also called solarblind detectors, can detect very weak UV signals under intense background radiation. These devices have important applications including missile plume detection, chemical/biological agent sensing, flame alarms, covert space-to-space and submarine communications, ozone-layer monitoring, and gas detection. Due to their high responsivity (600 A/W), high speed, high cathode gain (on the order of a million), and low dark current properties, photomultiplier tubes (PMTs) are frequently used in such applications. However, PMTs are very expensive and bulky. Besides, they require a cooling system, and they have high operation voltages in excess of 1000 V. To achieve solar-blind detection, PMTs should also be integrated with complex and expensive filters. In order to avoid these disadvantages, high performance solid-state UV photodetectors with high internal gain are needed. Wide band-gap semiconductor photodetectors, such as $Al_xGa_{1-x}N$ with $x=0.4$, are ideal candidates for this purpose. These devices are intrinsically solar blind, in which no additional filters are needed, they have low noise, and fast response times. The lack of high internal gain has been the major limitation for the usage of AlGaN photodetectors for applications that require high sensitivity detectors. There have been several theoretical research works that examined the avalanche effect in GaN and AlGaN-based structures. However, reproducible high gain in AlGaN-based APDs is still a major limitation. We have designed, fabricated, GaN/AlGaN based photodetectors, and according to characterization measurements, the Schottky, p-i-n, and avalanche detectors have high performance in terms of quantum efficiency, dark current, detectivity, high speed response, and high reproducible avalanche gain.

Keywords: Photodetectors, AlGaN, GaN, Avalanche, high gain.

ÖZET

PMT PERFORMANSINI GEÇEN GaN/AlGaN-TABANLI UV FOTODEDEKTÖRLER

Turgut Tut
Fızık Doktora
Tez Yöneticisi : Prof. Dr. Ekmel Özbay

Eylül 2008

Yakın zamandaki yüksek oranda Al ihtiva eden Al*x*Ga1−*x*N materyal büyütme teknolojisi ışığın ultraviole dalga boylarında çalışan iyileştirilmiş sensitivite, düşük gürültülü, düşük karanlık akım yoğunluğuna sahip, yuksek hızlı AlGaN tabanlı yüksek performanslı Schottky, p-i-n, ve (metal-yarıiletken-metal) MSM, tipi fotodetektörleri üretmeyi mümkün kılmıştır ve bu tür detektörler imal edilmiştir. Atmosferdeki ozon moleküllerinin ultraviole ışığı 280 nm dalga boyundan küçük değerler için filtrelemesi sayesinde bu dalga boylarındaki güneşten gelen radyasyon dünya yüzeyine ulaşmasını engeller. Bu durum sayesinde, 280 nm civarındaki dalga boyuna sahip kırılma dalga boyundaki UV fotodedektörler ki güneş-körü dedektörler olarak da adlandırılırlar, çok zayıf UV sinyalleri bile algılayabilirler. Bu aygıtlar misil füze uyarı sistemleri, kimyasal/biyolojik ajan tanıma, yangın alarmları, uzay ve denizaltı haberleşmesi, ozon tabakasının durumunu kontrol etme, gaz algılama gibi önemli uygulama alanlarına sahiptirler. Yüksek responsiviteye sahip olması hasebiyle (600 A/W), yüksek hızlı, yüksek katod verimine sahip (milyon mertebesinde), ve düşük karanlık akımlı, foton yükseltici tüpler (FYT'ler) bu tür uygulamalar için kullanılmaktaydı. Fakat, FYT'ler pahalı ve hantal yapıdadırlar. Ayrıca bunun yanında, çalışmak için soğutucu bir sisteme ve çok yüksek voltajlara (1000V) ihtiyaç duyarlar. Ayrıca bu aygıtlar güneş-körü algılama yapabilmek için kompleks ve pahalı filtrelerle beraber kullanılırlar. Bu dezavanlatajlardan sakınmak için bunların yerine yüksek performanslı yarıiletken dedektörler kullanılmalıdır. Geniş bantlı yarı iletken olan $Al_xGa_{1-x}N$ (x=0.4) tabanlı fotodedektörler bunun için ideal adaylardırlar. Bu aygıtlar yapısı itibariyle güneş körüdürler bu nedenle filtreye ihtiyaç duymazlar, düşük gürültüye ve hızlı fotocevaba sahiptirler. Bu dedektörlerin önündeki en büyük engel ise bu dedektörler çok yüksek içsel kazanca sahip değildirler. Şimdiye kadar bir kaç gurup GaN ve AlGaN tabanlı dedektörlerdeki çığ etkisini teorik olarak incelemişlerdir. Lakin, tekrarlanabilir yüksek kazançlı cığ etkisi ile çalışan fotodedektör üretmek hala çok zordur. Biz gurup olarak kuvantum verimi, karanlık akım, dedektivite, yüksek hız, yüksek tekrarlanabilir çığ verimi açısından yüksek performansa sahip Schottky, p-i-n, ve çığ etkili dedektörleri dizayn ettik, urettik ve karakterızasyonunu yaptık.

Anahtar Kelimeler: Fotodedektörler, AlGaN, GaN, Avalanş (çığ etkisi), yüksek kazanç

Acknowledgements

I would like to express my deepest gratitude to my supervisor Prof. Ekmel Ozbay for his invaluable guidance, motivation, encouragement, confidence, understanding, and endless support. It has been an honor for me to work with him, and I learned a lot from his superior academic personality.

I also thank the members of the thesis committee, Asst. Prof. Ali Kemal Okyay, Asst. Prof. Ceyhun Bulutay, Assoc. Prof. Oğuz Gülseren, Prof.Dr. Süleyman Özçelik for their useful comments and suggestions.

I would like to thank all the former and present members of Advanced Research Laboratory for their continuous support. Thank you all, members of the Physics and EE Engineering department for making life easier and enjoyable. I want to especially thank the group members of the detector research team: Necmi Bıyıklı, Mutlu Gökkavas, Bayram Bütün, Serkan Bütün, Tolga Kartaloğlu, İbrahim Kimukin, Erkin Ülker, Tolga Yelboğan. Without them, this work would not be complete. It was a pleasure to work with these hard-working people in the same group. I also want to thank to Murat Güre and Ergün Kahraman for their technical help and keeping our laboratory in good condition.

I would like to thank Mehmet Bayındır, Aşkın Kocabaş, Coşkun Kocabaş, Sinem Binicioğlu Çetiner, Ender Çetiner, Onur Kılıç, Muhammed Acar, Özgür Kelekçi , Kamil Boratay Alıcı, Kaan Güven for their company, moral support and help during my graduate study.

Finally I would like to express my endless thank to my family for their understanding and continuous moral support.

Table of Contents

List of Figures

List of Tables

Chapter 1

Introduction

The recent developments in high Al-content $Al_xGa_{1-x}N$ material growth technology made it possible to fabricate high performance solar-blind photodetectors operating in the ultraviolet (UV) spectral region with improved receiver sensitivity, low noise, low dark current density, and high speed AlGaN based Schottky [1,2], p-i-n [3,4], and metal-semiconductor-metal photodetectors [5] with very high performances have already been demonstrated. The UV-filtering nature of the atmospheric ozone molecules blocks the solar radiation to reach the earth's surface for wavelengths shorter than 280 nm. In this case, UV photodetectors with cutoff wavelengths around 280 nm, which are also called solar-blind detectors, can detect very weak UV signals under intense background radiation. These devices have important applications including missile plume detection, chemical/ biological agent sensing, flame alarms, covert space-to-space and submarine communications, ozone-layer monitoring, and gas detection. Due to their high responsivity (600 A/W), high speed, high cathode gain (on the order of a million), and low dark current properties, photomultiplier tubes (PMTs) are frequently used in such applications. However, PMTs are very expensive and bulky. Besides, they require a cooling system, and they have high operation voltages in excess of 1000 V. To achieve solar-blind detection, PMTs should also be integrated with complex and expensive filters. In order to avoid these disadvantages, high performance solid-state UV photodetectors with high internal gain are needed [6,7]. Wide band-gap semiconductor photodetectors, such as $Al_xGa_{1-x}N$ with x=0.4, are ideal candidates for this purpose. These devices are intrinsically solar blind, in which no additional filters are needed, they have low noise[8], and fast response times[9]. The lack of high internal gain has been the major limitation for the usage of AlGaN photodetectors for applications that require high sensitivity detectors. There have been several theoretical research work that examined the avalanche effect in GaN and AlGaN-based structures [10,11,12]. Experimental work on both GaN [13,14, 15,16,17,18,19] and AlGaNbased [20,21,22] avalanche photodiodes (APDs) were also reported. We have designed, fabricated, and according to characterization measurements, the Schottky, p-i-n, and avalanche detectors have high performance in terms of quantum efficiency, dark current, detectivity, high speed response, and high reproducible avalanche gain.

Chapter 2

THEORETICAL BACKROUND

This chapter gives a brief explanation to the basic operation principles of a photodetector especially APDs and the design basics for the optical simulations. We will first explain the theoretical background for a p-n junction, Schottky diode, and p-i-n diodes. Also the criteria for a good photodiode are discussed namely quantum efficiency and bandwidth.

Photodetectors can be separated into two classes: quantum detectors and thermal detectors. Thermal detectors respond to heating caused by absorption of the incident radiation. The first requirement for thermal detectors is that the heating effect results in a temperature change. Also, this temperature change should yield a measurable change in a physical parameter such as resistance, capacitance etc. Thermopile, bolometer, pyroelectric, golay cell, superconductor detectors are examples of thermal detectors. Thermal detectors can operate in a very broad spectral range. However, their bandwidth and sensitivity performances are relatively poor. The operation of quantum detectors is based on the photo-effect, in which the absorption of photons by some materials results in an electronic transition to a higher energy level and the generation of mobile charge carriers. Under the effect of an electric field these carriers move and produce a measurable electric current. Photoemissive, photoconductive, and photovoltaic detectors are in this category. They have limited spectral response, but demonstrate high sensitivity and high speed which are very important for optical communication systems. In photoconductive detectors, when photons are absorbed by a semiconductor material, mobile charge carriers are generated (an electron-hole pair for every absorbed photon). The electrical conductivity of the material increases in proportion to the photon flux. An electric field applied to the material by an external voltage source causes the electrons and holes to be transported. This results in a measurable electric current in the circuit. As with photoconductive detectors, photovoltaic detectors are also known as photodiodes rely on photo-generated charge carriers for their operation. A photodiode is simply a p-n junction whose reverse current increases when it absorbs photons. p-n, p-i-n, schottky photodiodes, avalanche photodiodes (APD) are widely used photodetectors. When we apply a reverse bias high enough across a p-n junction, due to high electric field in the depletion region on the order of $10^6 V/cm$ can cause electrons to impact-ionize and this results in avalanche gain. Avalanche photodiodes can be used instead of photomultiplier tubes in photon counting applications. Operating principles of schottky and p-i-n photodiodes are discussed in the following sections.

2.1 Photodiode operation

When light incident on a junction of a photodiode, photons having energy larger than or equal to bandgap energy of the semiconductor are absorbed and excess electron-hole pairs are created and then separated by the established electric field in the depletion region. Once the photodiode is connected through an external load in a circuit, a measurable current flows through the circuit which is proportional to the number of photons absorbed and the photo-generated carriers.

Schottky photodiodes

The theory of rectification in metal-semiconductor junction was developed in 1930 by W. Schottky who attributed rectification to a space-charge layer in the semiconductor. A schottky barrier is composed of metal and semiconductor which is brought into intimate contact. When metal is deposited on a semiconductor in the thermal equilibrium, the Fermi levels of the two materials must be coincident. The energy band diagram can be seen in Figure 2.1.

The work function is the energy difference between the vacuum level and the Fermi level. This quantity is denoted by $q\varphi m$ for the metal and equal to $q(\chi + V n)$ for the semiconductor. The potential difference between the metal and the semiconductor work functions is called the contact potential. $q\varphi Bn$ is called the barrier height and is equal to $q(\varphi m - \chi)$. Under the abrupt junction approximation that $\rho \approx qN_D$ for $x < W$,

$$W = \sqrt{\frac{2\varepsilon}{qN_D}(Vbi - V)}$$

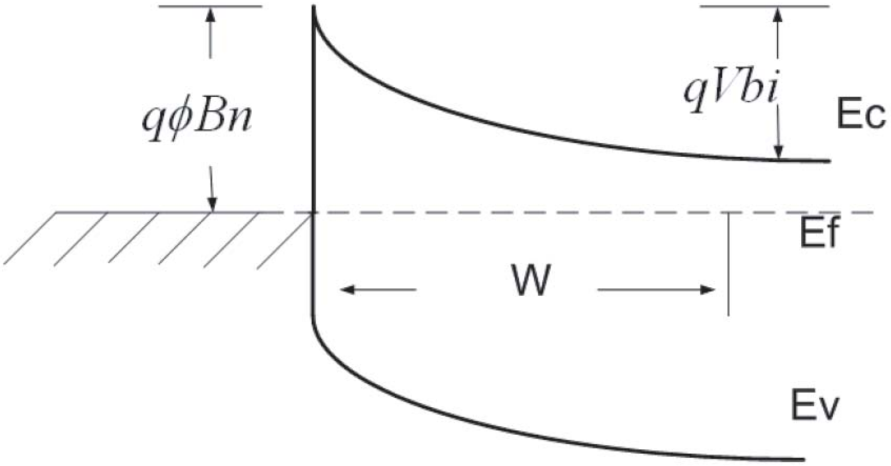

Figure2.1.1 Energy band diagram of a Schottky contact

Here ε is the dielectric constant of the semiconductor, N_D is the ionized donor atom density, Vbi is the built-in potential in the semiconductor, and the V is the applied potential to the junction. The current transport in the metal-semiconductor contacts is mainly due to majority carriers, in contrast to p-n junctions. There are mainly four different transport mechanisms: thermionic emission over the barrier, tunneling through the barrier, carrier recombination or generation in the depletion region, carrier recombination in the neutral region of the semiconductor. Thermionic emission is the dominant transport mechanism, which gives rise to the ideal diode characteristics. Thermionic emission theory is derived by Bethe for high-mobility semiconductors, and diffusion theory is derived by Schottky for low-mobiliy semiconductors. Finally, a synthesis of the two approaches has been proposed by Crowell and Sze. The complete expression of the J-V characteristics is given by the following equations.

$$J = J_s(e^{\frac{qV}{kT}} - 1)$$

$$J_s = A^{**}T^2 \exp(-\frac{q\phi B_n}{kT})$$

Schottky photodiodes can be used for detecting UV and visible radiation and are the fastest of photodiodes available. However they have low quantum efficiency due to thin absorption regions and the highly absorbing schottky metal. Applying sufficiently high reverse bias voltages, the whole N- region (active region) can be depleted, resulting in a continuous electric field across the region. Photons with energies larger than the band gap are absorbed in the depletion region and electron-hole pairs are generated. The generated electron- hole pairs are swept away by the electric field. Electrons drift to the N+ doped semiconductor, holes drift to Schottky metal and an output current develops in the external circuit. The transport of carriers can be described using the diagram in Figure 2.1.2. The depletion region can be considered as a parallel plate capacitor with a capacitance C = εA/d where ε is the dielectric constant, A is the diode area, and d is the depletion layer width. At steady state, the voltage bias on the capacitor is V_0, which results in a steady state total charge of Q_0 across the capacitor, $Q_0 = CV_0$. The electric field E varies with distance in depletion region so we can express the applied bias voltage as,

$$V_0 = \int_0^d E(x)dx$$

Here we assume that all the applied voltage appears across the depletion region. Let's assume that, at t=0, a narrow optical pulse generates carriers with a total charge of q, at x_0 from the Schottky contact as in Figure 2.1.4. Because of the established built-in electric field in the depletion region, electrons and holes drift in opposite directions in the form of charge sheets having surface charge density σ = q/A. The negatively charged sheet composed of electrons move away from the Schottky contact with with drift velocity Ve, and positively charged sheet composed of holes move towards the Schottky contact with drift velocity Vh. Each sheet contributes to the electric field formed between the sheets in equally as,

$$E_\sigma = \frac{\sigma}{\varepsilon}$$

And this electric field is opposite to the depletion layer electric field, which results in a voltage drop across the depletion region as the charged sheets move away from each other. This time dependent voltage can be expressed as:

$$V_\sigma = \int_{xh(t)}^{xe(t)} E_\sigma dx = E_\sigma \left[xe(t) - xh(t) \right]$$

$$Xh(t) = X_0 - \upsilon_h(t), \quad 0<\mathrm{t}<\mathrm{t}_h$$

$$Xe(t) = X_0 + \upsilon_e(t), \quad 0<\mathrm{t}<\mathrm{t}_\mathrm{e}$$

where $t_e = \dfrac{d - x_0}{\upsilon_e}$ and $t_h = \dfrac{x_0}{\upsilon_h}$ are electron and hole transit time, defined as the time required for the carriers to complete their transport. Assuming $t_e > t_h$, we can express the potential drop caused by the charge sheets as:

$$V_\sigma = \begin{Bmatrix} \dfrac{\sigma}{\varepsilon}(\upsilon_e + \upsilon_h)t & 0<\mathrm{t}<t_h \\ \dfrac{\sigma}{\varepsilon}\upsilon_e t & t_h<\mathrm{t}<te \end{Bmatrix}$$

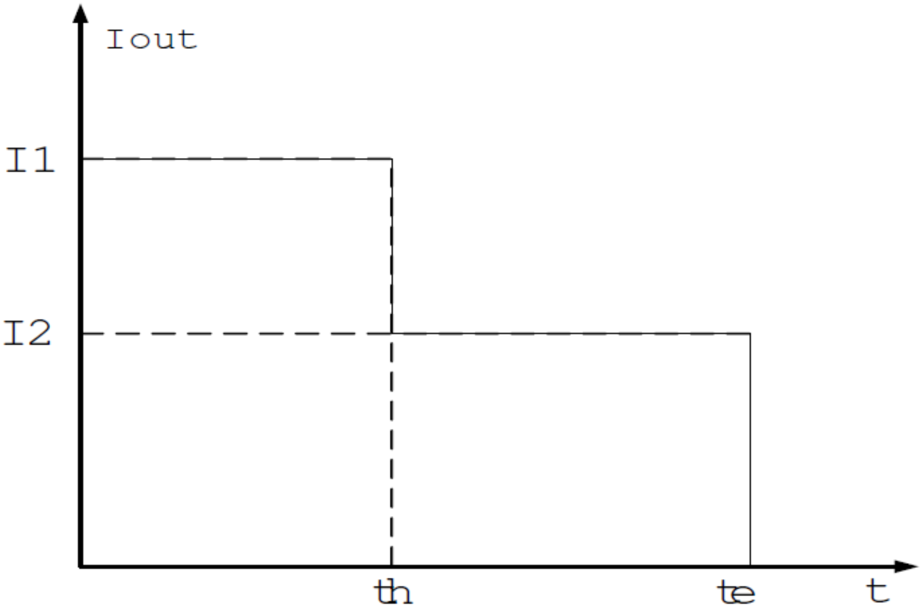

Figure 2.1.2 Time dependence waveform of the induced current.

$I_{out}(t) = \dfrac{dQ(t)}{dt} = \dfrac{d}{dt}\left[CV(t)\right]$ where $V(t) = V_0 - V_\sigma$ so $I_{out}(t)$ is;

$$I_{out}(t) = \begin{Bmatrix} I_1 = \dfrac{q}{d}(\upsilon_e + \upsilon_h) & 0<\mathrm{t}<t_h \\ I_2 = \dfrac{q}{d}\upsilon_e & t_h<\mathrm{t}<te \end{Bmatrix}$$

Using this result we can get the output current for different absorption situations. We can assume that the absorption over the depletion layer is constant, and the hole drift velocity is smaller than electron drift velocity. Under this assumption, when all electrons reach the end of the depletion layer, there exist some holes that contribute to the total current. Therefore, the current flows until all the holes leave the depletion layer. Current output of such a device can be seen in Figure 2.1.3. We can also assume that the absorption constant is so high that all the incident light is absorbed near the Schottky contact. In this case the current output is a square that continues until te .

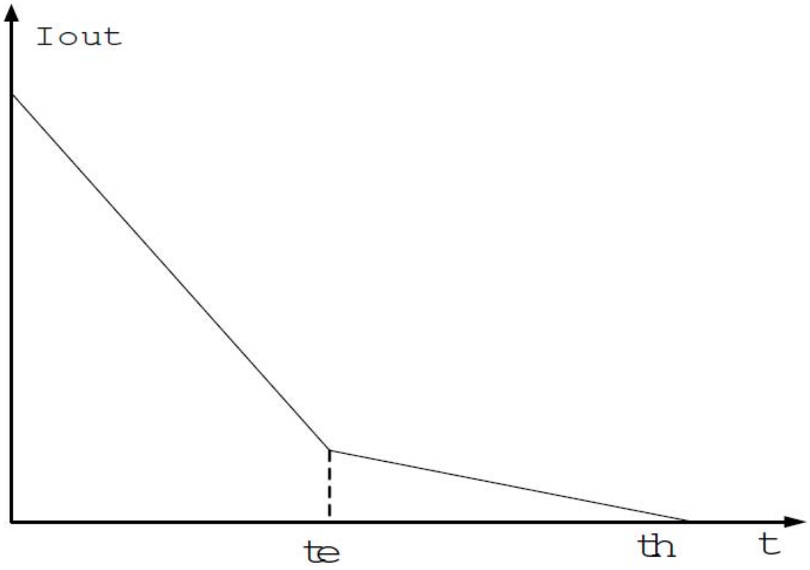

Figure 2.1.3 Expected waveform of output current of a photodiode where hole drift velocity is smaller than electron drift velocity.

P-I-N Photodiodes

A p-i-n photodiode is simply a p-n junction with an intrinsic layer sandwiched between p and n type doped layers. It operates in reverse bias mode and it is suitable for high quantum efficiency operation due to its intrinsic layer. However, generally homojunction p-i-n photodiodes lack in high-speed operation because there is a diffusion component in the output current. The photo-generated carriers outside the depletion region diffuse into the intrinsic i region and in the depletion region they are swept away by the electric field. Since diffusing is slower than drifting in high electric field, p-i-n photodiodes are much slower than Schottky photodiodes. This problem can be solved by using p and n layers which have higher band gaps than intrinsic layer so that photo-generation occurs only in the intrinsic region. In this way, high efficiency and high speed p-i-n photodiodes can be designed.

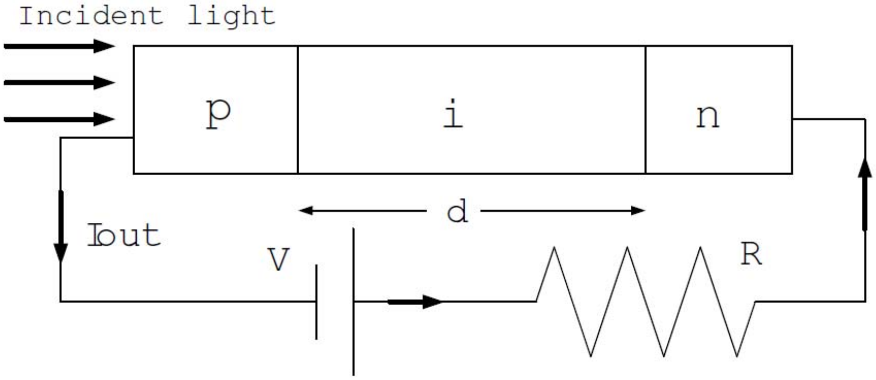

Figure 2.1.4 Schematics of a p-i-n photodiode

Avalanche photodiodes

An avalanche photodiode (APD) operates by converting each detected photon into a cascade of moving carrier pairs. With APDs, we have large photocurrent in the external circuit compared to the photo-generated photocurrent resulting from a very weak optical signal. By impact ionization process under high electric field, we have internal gain in the depletion region. For the avalanche multiplication to occur devices are operated at high voltages in the breakdown region usually avoided in normal operation.

The high electric field in the depletion region accelerates the photo-generated charges, causing them to have kinetic energy large enough to ionize the crystal lattice with the resulting new electron-hole pairs. The new charge carriers are also accelerated and avalanche multiplied as well.

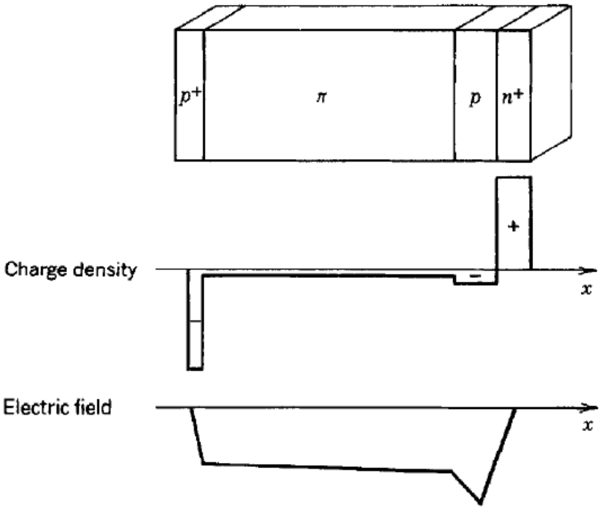

Figure 2.1.5 Reach-through p+-π-p-n+ APD structure. The π region is very lightly doped p-type material.The p + and n + regions are heavily doped [23].

Since during the avalanche process, we have high electric field in the depletion region, APDs are fast devices compared to other devices with internal gain. In a material with avalanche gain, the impact ionization can be described by the ionization coefficients alpha and beta of electron and hole which is defined as the number of new pairs generated for unit length by the carrier under a certain electric field. The inverse of alpha and beta are the ionization lengths and represent the mean free path between successive multiplications. The ionization coefficients increase with the electric field in the depletion region and decreases with the device temperature.

Ionization ratio can be defined as the ratio of the ionization coefficients and symbolized with the letter k. When k is very small this means that holes do not ionize substantially with regard to electrons so most of the ionization is realized by electrons. The multiplication terminates when all of the electrons reach the n side of the depletion layer. However, if the k is close to 1, there will be a positive feedback and we have an enormous gain. This is, on the other hand, is not desirable for the following reasons. It takes more time for the hole to process this in turn decreases the bandwidth. Device noise increases because the process is intrinsically random. Since we have very high gain, the device is unstable and this causes the device to get into avalanche breakdown.

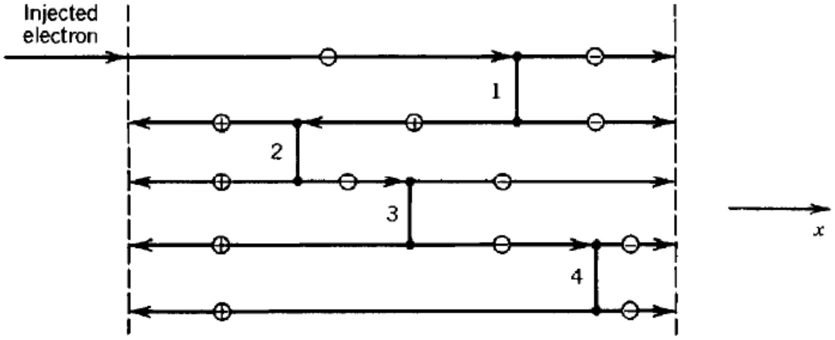

Figure 2.1.6Constancy of the sum of the electron and hole current densities across a plane at any x. By way of illustration, four impact ionizations and five electrons-plus-holes crossing every plane are illustrated [23].

It is advantages to use materials in the APD structures having k values either close to 0 or very large. For instance, if material favors the electrons with regards to impact ionization, optimal gain is achieved when the electrons are injected at the p-type layer of the depletion layer.

We will first consider the simpler problem of single-carrier (electron) multiplication ($\alpha_h = 0 , k = 0$). Let $J_e(x)$ be the electric current density carried by electrons at location x, as shown in the figure. Within a distance dx, on the average, the current is incremented by the factor,

$dJ_e(x) = \alpha_e J_e(x)dx$,

From which we obtain the differential equation,

$$\frac{dJ_e}{dx} = \alpha_e J_e(x),$$

Whose solution is the exponential function $J_e(x) = J_e(0)\exp(\alpha_e x)$. The gain $G = J_e(W) / J_e(0)$ is therefore

$$G = \exp(\alpha_e W).$$

The electric current density increases exponentially with the product of the ionization coefficient α_e and the multiplication layer width W.

The double-carrier multiplication problem requires knowledge of both the electron current density $J_e(x)$ and the hole current density $J_h(x)$. It is assumed that only electrons are injected into the multiplication region. Since hole ionizations also produce electrons, however, the growth of $J_e(x)$ is governed by the differential equation.

$$\frac{dJ_e}{dx} = \alpha_e J_e(x) + \alpha h J_h(x),$$

As a result of charge neutrality, $dJ_e / dx = -dJ_h / dx$, so that the sum $J_e(x) + J_h(x)$ must remain constant for all x under steady-state conditions. This is clear from fig.; the total number of charge carriers crossing any plane is the same regardless of position,

Since it is assumed that no holes are injected at $x = W$, $J_h(W) = 0$, so that

$$J_e(x) + J_h(x) = J_e(W),$$

The hole current density $J_h(x)$ can therefore be eliminated in the equation to obtain

$$\frac{dJ_e}{dx} = (\alpha_e - \alpha_h)J_e(x) + \alpha_h J_e(W).$$

The first-order differential equation is readily be solved for the gain $G = J_e(W) / J_e(0)$.

For $\alpha_e \neq \alpha_h$ the result is $G = (\alpha_e - \alpha_h) / \left\{ \alpha_e \exp\left[-(\alpha_e - \alpha_h) W \right] - \alpha_h \right\}$, from which we obtain

$$G = \frac{1-k}{\exp\left[-(1-k)\alpha_e W \right] - k}.$$

The single-carrier multiplication result for gain, with its exponential growth, is recovered when k=0. When k is infinity, the gain remains unity because only the electrons are injected and electrons do not multiply. For k=1, the equation becomes indeterminate and gain must be obtained directly from. The result is then $G = 1/(1 - \alpha_e W)$. Instability is reached when $\alpha_e W = 1$. The dependence of the gain on $\alpha_e W$ for several values of the ionization ratio k is illustrated in figure 2.1.7.

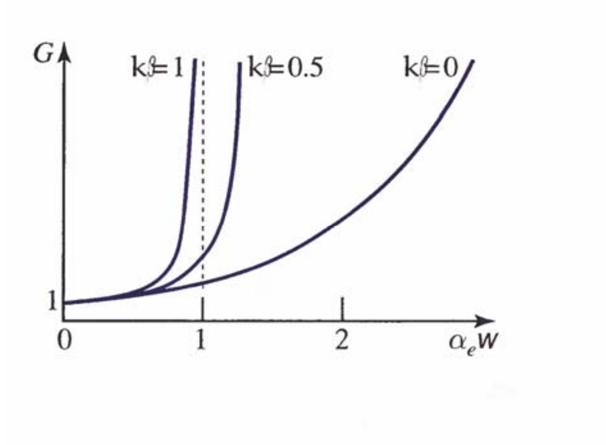

Figure 2.1.7 Growth of the gain G with multiplication-layer width for several values of the ionization ratio k, assuming pure electron injection [23].

Diode Characteristics

Photodiodes characterization composed of I-V (current-voltage) measurement, quantum efficiency, high speed (bandwidth) measurement. Performance of a photodiode is tested via these characterizations.

Current-Voltage Characteristics

Low dark current and high breakdown voltage are two parameters to test the photodiode quality. Dark current is the current flowing in the reverse bias with no illumination. A device with lower dark current is likely to be more sensitive. We cannot apply a reverse bias voltage as high as we like through a photodetector because after a certain voltage photodiode enters into avalanche breakdown which puts a limit on the reverse bias voltage that can be applied for photodiode operation.

Quantum Efficiency

The quantum efficiency η ($0 \leq \eta \leq 1$) of a photodetector is defined as the probability that a single photon incident on the device generates a photo-carrier pair that contributes to the detector current. When many photons are incident, as is almost always the case, η is the ratio of the flux of generated electron-hole pairs that contribute to the detector current to the flux of incident photons. Not all incident photons produce electron-hole pairs because not all incident photons are absorbed. Some photons may be reflected from the surface of the photodetector, or photo-generated pairs near the surface recombine due to the abundant recombination centers and fail to contribute to the current. The quantum efficiency can therefore be written as,

$$\eta = (1-R)\varsigma\left[1-\exp(-\alpha d)\right]$$

where R is the front surface reflectivity, α is the power absorption coefficient, d is the thickness of the absorbing semiconductor layer, and ς is the fraction of electron-hole pairs that contribute to the detector current.

Bandwidth

As mentioned previously, the response time of a photodetector is mainly limited by the transit times of the photo-generated carriers. RC time constant of the photodiode circuit and diffusion of carriers in the undepleted regions also impose limitations on the response time of a photodetector.

Schottky and heterojunction photodetector designs can be used to resolve the carrier diffusion problem either by decreasing the undepleted regions as in Schottky diodes or using different band gap materials as in heterojunction photodiodes.

The impulse-response function is determined by convolving i(t) with the exponential function $(1/RC)\exp(-t/RC)$.When we decrease d (depletion width), the capacitance of the junction increases. Transit time also decreases when we decrease d. The transit times and capacitance limited 3-dB bandwidths can be written as:

$$f_{tr} = 0.45\frac{\upsilon}{d}$$

$$f_{RC} = \frac{d}{2\pi R\varepsilon A}$$

By decreasing d we can increase bandwidth as long as we use small devices so that the capacitance of the devices decreases accordingly. So if we consider only transit time limitation, bandwidth of the photodetector is inversely proportional to d.

Bandwidth-Efficiency Trade-off

The bandwidth-efficiency product determines the overall performance of a photodiode. Bandwidth and efficiency have inverse dependencies on active layer thickness, d. High quantum efficiencies near unity and bandwidth can be achieved with very thick and very thin active layers respectively but their product for a given d is almost constant. To increase bandwidth-efficiency product, we have to make use of resonant cavity enhancement effect (RCE).

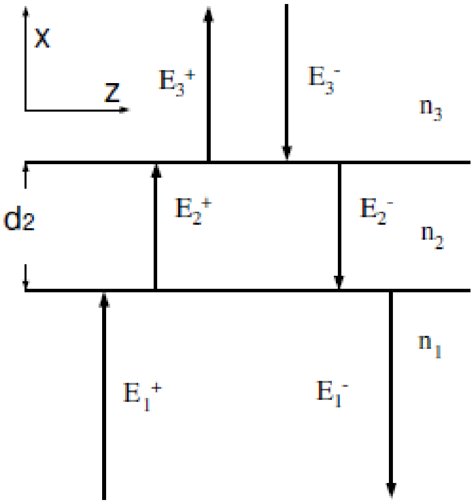

Figure 2.2.1 Reflection and transmission of an electromagnetic wave incident on a dielectric film of thickness *d*2.

2.2 Optical Design using TMM code

In this chapter, we will explain the optical simulation of our photodetector designs using TMM (Transfer matrix multiplication) code.

Assuming the incident light is in the form of polarized plane waves and it is vertical to the plane of interface between the two media, we can write the electric field vector as,

$$E = E_0 e^{(\omega t - i\vec{k}\bullet\vec{r})}$$

Therefore we can write the electric fields in three regions as the following.

$$\vec{E} = \left\{ \begin{array}{ll} \hat{y}E_1^+ e^{-ik_1x} + \hat{y}E_1^- e^{ik_1x}; & x<0 \\ \hat{y}E_2^+ e^{-ik_2x} + \hat{y}E_2^- e^{ik_2x}; & 0<x<d_2 \\ \hat{y}E_3^+ e^{ik_3d_2} e^{-ik_3x} + \hat{y}E_3^- e^{ik_3d_2} e^{ik_3x}; & x>d_2 \end{array} \right\}$$

$$k_i = (\frac{\omega}{c})n_i = k_0 n_i; \quad i = 1,2,3$$

n_1, n_2, and n_3 are refractive indices and

$k_0 = \frac{\omega}{c} = \frac{2\pi}{\lambda_0}$ denotes the free space wave number. The implicit $e^{i\omega t}$ dependence has been suppressed and therefore the superscripts + and – correspond to waves propagating in the +x and –x directions respectively.

The corresponding magnetic fields can be calculated by using the formula,

$$\vec{H} = \vec{k}x\frac{\vec{E}}{\omega\mu}$$

And are given by

$$\vec{H} = \left\{ \begin{array}{ll} \hat{z}\frac{n_1}{c\mu_0}E_1^+ e^{-ik_1x} - \hat{z}\frac{n_1}{c\mu_0}E_1^- e^{ik_1x}; & x<0 \\ \hat{z}\frac{n_2}{c\mu_0}E_2^+ e^{-ik_2x} - \hat{z}\frac{n_2}{c\mu_0}E_2^- e^{ik_2x}; & 0<x<d_2 \\ \hat{z}\frac{n_3}{c\mu_0}E_3^+ e^{ik_3d_2} e^{-ik_3x} - \hat{z}\frac{n_3}{c\mu_0}E_3^- e^{ik_3d_2} e^{ik_3x}; & x>d_2 \end{array} \right\}$$

Where the media are assumed to be nonmagnetic with $\mu = \mu_0$. Since both E and H represent tangential components, they must be continuous at x=0 and at x=d_2. Continuity at x=0 gives,

$$E_1^+ + E_1^- = E_2^+ + E_2^-,$$

$$n_1(E_1^+ - E_1^-) = n_2(E_2^+ - E_2^-),$$

$$\begin{pmatrix} E_1^+ \\ E_1^- \end{pmatrix} = S_1 \begin{pmatrix} E_2^+ \\ E_2^- \end{pmatrix} = \frac{1}{t_1}\begin{pmatrix} 1 & r_1 \\ r_1 & 1 \end{pmatrix}\begin{pmatrix} E_2^+ \\ E_2^- \end{pmatrix},$$

Where r$_1$ and t$_1$ are the amplitude reflection and transmission coefficients at the first interface and given by

$$r_1 = \frac{n_1 - n_2}{n_1 + n_2}$$

$$t_1 = \frac{2n_1}{n_1 + n_2}$$

Continuity of the fields at x=d$_2$ gives,

$$\begin{pmatrix} E_2^+ \\ E_2^- \end{pmatrix} = S_2 \begin{pmatrix} E_3^+ \\ E_3^- \end{pmatrix} = \frac{1}{t_2}\begin{pmatrix} e^{i\delta_2} & r_2 e^{i\delta_2} \\ r_2 e^{-i\delta_2} & e^{-i\delta_2} \end{pmatrix}\begin{pmatrix} E_3^+ \\ E_3^- \end{pmatrix}$$

Where r$_2$ and t$_2$ are the amplitude reflection and transmission coefficients at the second interface

$\delta_2 = k_2 d_2 = k_0 n_2 d_2$ then we can combine equations

$$\begin{pmatrix} E_1^+ \\ E_1^- \end{pmatrix} = S \begin{pmatrix} E_3^+ \\ E_3^- \end{pmatrix} = \begin{pmatrix} a & b \\ c & d \end{pmatrix}\begin{pmatrix} E_3^+ \\ E_3^- \end{pmatrix}$$

Now in the third medium there will not be any reflected wave and as such $E_3^- = 0$. This immediately gives us,

$$E_1^+ = aE_3^+$$

$$E_1^- = cE_3^+$$

And therefore the amplitude reflection and transmission coefficients of the film are given by

$$r = \frac{E_1^-}{E_1^+} = \frac{c}{a}$$

$$t = \frac{E_3^+}{E_1^+} = \frac{1}{a}$$

$$R = |r|^2 = \frac{r_1^2 + r_2^2 + 2r_1 r_2 \cos 2\delta_2}{1 + r_1^2 r_2^2 + 2r_1 r_2 \cos 2\delta_2}$$

$$T = |t|^2 \frac{n_3}{n_1} = \frac{n_3}{n_1} \frac{t_1^2 t_2^2}{1 + r_1^2 r_2^2 + 2r_1 r_2 \cos 2\delta_2}$$

Upon substituting the related values for r and t, we obtain

$$R + T = 1$$

Furthermore when $\cos 2\delta_2 = -1$, i.e., when $\delta_2 = (m + \frac{1}{2})\pi$; m=0,1,2,... or $d_2 = \frac{\lambda_0}{4n_2}, \frac{3\lambda_0}{4n_2}, \frac{5\lambda_0}{4n_2}, ...$ minimum reflectivity is achieved (for $r_1 r_2 > 0$) and it is given by,

$$R = \left(\frac{r_1 - r_2}{1 - r_1 r_2} \right)^2 = \left(\frac{n_1 n_3 - n_2^2}{n_1 n_3 + n_2^2} \right)^2$$

Thus the reflectivity will be zero when $n_2 = (n_1 n_3)^{\frac{1}{2}}$. The reflectivity of the surface can be made zero at any chosen wavelength λ_c by choosing the film thickness to be $\frac{\lambda_c}{4n_2}$. This technique of reducing the reflectivity of a surface is known as blooming and the surface is said to be anti-reflected coated.

When $\cos 2\delta_2 = 1$, i.e., when $d_2 = \frac{\lambda_0}{2n_2}, \frac{2\lambda_0}{2n_2}, \frac{3\lambda_0}{2n_2}, ...$ the reflectivity is given by

$$R = \left(\frac{n_3 - n_1}{n_3 + n_1} \right)^2$$

which is independent of the refractive index of the intermediate film.

For the case of two films, with r_3 and t_3 are the amplitudes of reflection and transmission coefficients between media 3 and 4 and

$$\delta_3 = k_3 d_3 = k_0 n_3 d_3$$

Thus

$$\begin{pmatrix} E_1^+ \\ E_1^- \end{pmatrix} = S \begin{pmatrix} E_4^+ \\ E_4^- \end{pmatrix}$$

where $S = S_1 S_2 S_3$

Similarly one can obtain expressions for the reflectivity and transmittivity. Generalizing the above analysis for N films and for oblique incidence, we may write

$$\begin{pmatrix} E_1^+ \\ E_1^- \end{pmatrix} = S \begin{pmatrix} E_{N+2}^+ \\ E_{N+2}^- \end{pmatrix}$$

where $S = S_1 S_2 S_3 .....S_{N+1}$

and

$$S_j = \frac{1}{t_j} \begin{pmatrix} e^{i\delta_j} & r_j e^{i\delta_j} \\ r_j e^{-i\delta_j} & e^{-i\delta_j} \end{pmatrix}$$

and $\delta_1 = 0$

$$\delta_j = k_j d_j \cos\theta_j = \left(\frac{2\pi}{\lambda_0}\right) n_j d_j \cos\theta_j ; j = 2,3,4,...,(N+1)$$

and rj and tj are the amplitude reflection and transmission coefficients between media with refractive indices nj and nj+1.

Using snell's law, δ_j can also be expressed as,

$$\delta_j = \left(\frac{2\pi}{\lambda_0}\right) d_j (n_j^2 - n_1^2 \sin^2\theta_1)^{\frac{1}{2}} .$$

This method can be used to calculate the transmission, reflection and absorption at any layer and is called the transfer matrix method (TMM).

Distributed Bragg Mirrors (DBR's) are widely used in optoelectronic applications such as detectors and semiconductor lasers. A DBR is a stack consisting of periodically alternating quarter-wave thick material layer pairs whose refractive indices are different at the wavelength region of interest. Each pair consists of two layers having thicknesses of $\lambda_c / 4n_1$ and $\lambda_c / 4n_2$ respectively and λ_c is the central wavelength of the mirror where reflectivity is maximum. All the light reflected from different interfaces of the DBR has the same phase resulting in constructive interference therefore we have very high reflectivity. Using TMM method for a DBR consisting of N pairs, the reflectivity at the center wavelength can be expressed as,

$$R_{\max} = \left(\frac{n_1^{2N} - n_2^{2N}}{n_1^{2N} + n_2^{2N}} \right)^2$$

This formula is valid when the stack is in the air, but for the first and the last layers which are different than air, we have to modify the formula as,

$$R_{\max} = \left(\frac{\frac{n_0}{n_s}(\frac{n_L}{n_H})^{2N} - 1}{\frac{n_0}{n_s}(\frac{n_L}{n_H})^{2N} + 1} \right)^2$$ where n_0 and n_s are refractive indices of air and substrate medium. We assumed that the thickness of the substrate layer is infinite, since it is significantly thicker than the other layers in the wafer structure.

We can illustrate this situation by growing DBR pairs consisting of SiO_2 and Si_3N_4 since at 350nm Si_3N_4 is grown on SiO_2 to have an enhancement in reflectivity. The appropriate thickness for DBR layers can be calculated using the formula $\lambda_c / 4n$, where n is the layer's refractive index at λ_c. For $\lambda_c = 350nm$, this results in the thicknesses of 49.7 nm and 59.5 nm for Si_3N_4 and SiO_2 respectively. By increasing the number of DBR pairs, we can obtain reflectivities that are very close to unity.

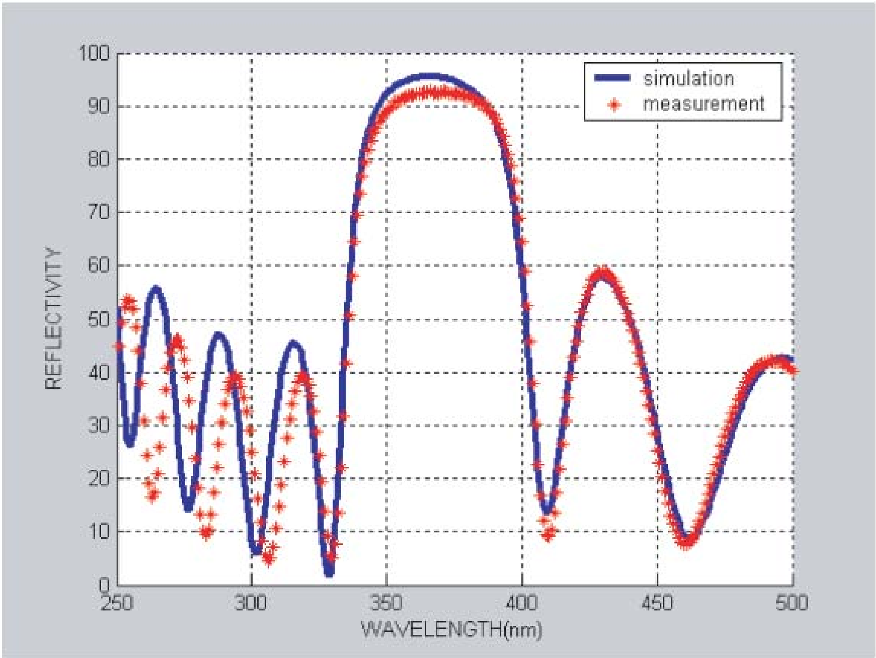

Figure 2.2.2 Reflectivity of 8 pairs of DBR on GaAs substrate.

The figure 2.2.2 shows the reflectivity of 8 pairs of DBR on GaAs substrate and it is close to unity.

Chapter 3

Fabrication and Characterization

In this chapter, fabrication processes and the characterization methods will be presented. Fabrications and characterizations were carried out in both Nanotechnology Research Center Lab and Advanced Research Lab at Bilkent University which has a class 100 clean room having a dust count of 100 particles per cubic foot volume. This corresponds to 3500 particles (with particles diameters of 0.5 micron or larger) per cubic meter.

Sample preparation

First, we have to obtain a sample large enough to handle with tweezer but not too large since the epitaxial wafers are very expensive. The mask size is 7x7 mm^2. The cleanness of the sample, the chemicals used, and the environment are very important for a successful fabrication. To cleave the wafer, we use a diamond tipped scriber-pen. After defining the line of the cut on the backside of the wafer which is not polished, we press the scribers tip at the edge of the wafer. Unfortunately it is not easy to obtain GaN, or AlGaN wafers in the desired size or shape. When the scriber's tip is pressed on the wafer, it may crack into various small pieces. Therefore, the samples are difficult to handle and process.

At the beginning of every step, we have to do a three-solvent-cleaning (TSC) process. Trichloroethane dissolves oil, acetone dissolves photoresist, organic molecules, and trichloroethane, and isopropanol dissolves acetone and water dissolves the acetone. Samples are placed into a teflon basket and immersed into a boiling trichloroethane for two minutes, then into acetone at room temperature for five minutes, then into boiling isopropanol for 2 minutes. Samples are exposed to the deionized water (DI) flow and then dried with a nitrogen gun.

Samples are baked on a hot plate at 120 °C for 2 minutes which called dehydration bake. Finally, the samples surfaces are examined under an optical microscope.

Normal photolithography

AZ 5214E type photoresist has an absorption peak at around 360 nm and we perform the UV exposure with an Hg lamp which has a line at 365 nm. Mask alignment is done with a Karl-Suss MJB3 mask aligner. Mask alignment is accomplished by means of alignment marks. After pre-bake, the sample is is aligned with the mask. Then the sample is exposed to the UV radiation for 20 seconds with an optical power of 8mW/cm^2 for a total dose of 160 mJ/cm^2.

Image Reversal Photolithography

In this technique the transparent parts of the mask will be transferred onto the resist, so that the mask is different from the mask used in normal lithography. The resist covered sample is aligned with the image-reversed mask and exposed with an optical power of 8mW/cm^2 for 8 seconds. Then the sample is baked for 2 minutes at 110 °C on a hot plate. The sample is exposed for 18 seconds without mask which is called flood exposure. These two additional processes change the photoresist so that the frst exposed regions behave as non-exposed regions and vice versa. Therefore the additional bake is very critical in image reversal lithography. The optimization is done by changing the image reversal bake time and the bake temperature. Image reversal photolithography makes the lift-off of thick metallization easy. Normally, the exposure is larger near the top of any resist, which results in a more rapid development near the surface and leads to a resist profile with a positive slope for positive resists. However, after image reversal this profile is also reversed, resulting in an undercut profile.

Development

AZ 400K developer is used with a 1:4 ratio of developer to DI water for the development of the exposed samples. In the normal photolithography the exposed regions of resist are etched while in the image reversal photolithography the non-exposed regions are etched. The development time is determined by using a dummy GaAs sample since we cannot observe the color change on a GaN or $Al_xGa_{1-x}N$ sample since it is transparent. In development, we use a white basket to observe the color change easily. When the color change has stopped, the samples are rinsed under DI water flow. By this method, we find the development time to be approximately 43-47 seconds with a thickness of 1.4micron. Then the sample is dried with a nitrogen gun. The samples are put under an optical microscope, the resolution patterns should be sharp and 1micron resolution should be observed for a good photolithography. Mask alignment is observed via the alignment marks.

Etching Techniques:

In processing of the wafer, we have to etch through the wafer surface. For example, we have to make contacts to an epitaxial layer buried under the surface of the wafer, second we must isolate devices by making mesas , third must make contacts to metalizations beneath the silicon nitride. Etching can be divided into wet (aqueous solution) etching and dry etching (Reactive Ion Etching).

Chemical etching techniques in liquid or gaseous environment is used to remove any barrier material not protected by hardened photoresist. The chemicals we choose depends on the material which we desire to etch. A high degree of selectivity is required so that the etchant will remove the unprotected areas much more rapidly than the photoresist layer. People use metals or other dielectric material as protection mask other than the photoresist.

Wet Chemical Etching

For silicon wafers, buffered oxide etch is commonly used to etch windows in silicon dioxide layers. BOE is a solution containing HF (hydrofluoric acid), and etching is performed by immersing the wafers in the solution. HF at room temperature etches silicon dioxide much more rapidly than it etches photoresist or silicon. The etch rates depend on the oxide density, acid density, and temperature so these parameters should be controlled for the desired etch depth.

Wet chemical etching is an isotropic process, etching equally in all directions. This "etch bias" is a serious problem in processes requiring linewidths with dimensions similar to the thickness of the film.

Chemical solvents are used to wet etch semiconductor and dielectric materials. GaAs etchant is frst to oxidize the surface with an oxidizing agent and second to remove the oxidized layer with acid or base. In our processes we use H2O2/NH3/H2O (2.4:8:300) as etchant with an etch rate of 50 *Angstrom/sec*. at room temperature. Dielectric materials SiO2, Si3N4 can be etched with HF. ITO can also be etched via *HF*. *HF* in aqueous form is very dangerous so we have to be very careful in using it. We use a dilute *HF* / DI water (1:30) in nitride etching at a rate of 400 Angstrom/sec.

Dry Etching

Dry etching is highly anisotropic process therefore, very anisotropic profiles can be obtained, without having the problem of undercutting problem which is a characteristic of wet etch processes. Dry etch processes need only small amount of reactant gases, on the other hand, wet etching results in disposal of a relatively large amounts of liquid chemical wastes.

Plasma etching immerses the wafers in a gaseous plasma created by RF excitation in a vacuum system. The plasma contains fluorine or chlorine ions which etch silicon dioxide. Sputter etching uses energetic noble gas ions such as Ar+ to bombard the wafer surface. Etching process occurs by physically knocking atoms off the surface of the wafer. Highly anisotropic etching can be obtained, but selectivity is not good. Metals can be used as barrier materials to protect the wafer from etching.

Reactive ion etching combines the plasma and sputter etching processes. Plasma systems are used to ionize reactive gases, and the ions are accelerated to bombard the surface. Etching process occurs through a combination of the chemical reaction and momentum transfer from the etching species.

In our system, we use ultra high vacuum RIE machine for dry etching. Photoresist and dielectric materials are etched with plasma ions hitting the sample surface. Using different gases in the plasma we can etch different materials. O2 is used to etch photoresist film. CCl2F2 etches SiO2, Si3N4, and ITO. Si3N4 can also be etched with CHF3. In our fabrication GaN and AlxGa$_{1-x}$N are etched with CCl2F2.

Photoreist removal

After windows are etched through the SiO2 layer, the photoresist is stripped from the surface, leaving a window in the silicon dioxide. Photoresist removal typically uses proprietary-liquid resist strippers, which cause the resist to swell and lose adhesion to the substrate surface. Dry etching may also be used to remove resist by oxidizing (burning process) it in oxygen plasma, a process which is often called resist ashing.

Metalization

In our processes we use the lift-off metallization technique to make ohmic and schottky contacts, and interconnects between them. Once the required metallization layout is defined by photolithography, the samples are coated by desired metals. Since the photoresist film has a finite thickness, the coated material (if it is thin enough) is discontinuous at the pattern edges of the resist. Therefore, in acetone the photoresist dissolves lifting off the material on it. The metals are deposited onto the samples via UHV LE590 box coater. Metals in powder or solid form are placed in tungsten boats. UHV causes the metal to evaporate in lower temperature.

Samples are placed over the boats. Short holder is used to decrease the usage of metals but we have to be careful watching the sensors display since the holder is half of the long holder the actual deposition rate is four times the displayed value. When the desired pressure is reached, current is passed through the tungsten boats and metal deposition takes place.

Annealing

To make metal semiconductor contacts ohmic we use rapid thermal process (RTP) in which samples are heated up to very high temperatures in very short time. Within 20-30 seconds, the metal contact melts and diffuses into the semiconductor and the barrier electrons encounter becomes very low as a result the contact resistance becomes ohmic. Flash lamps are used as the heating source. From the figure one can notice the cheese like structure on the ohmic contact which is an indicator of a good ohmic contact.

Plasma Enhanced Chemical Vapor Deposition (PECVD)

Dielectric films are used mainly to protect the devices on the wafer. Silicon nitride films can be used for passivating devices, because they serve as barriers to the diffusion of water and sodium. Silicon nitride oxidizes very slowly and prevents the underlying layers from oxidation. In our processes, PECVD is used to deposit silicon nitride and silicon oxide at relatively low temperatures with respect to other methods otherwise high temperature can affect the ohmic contacts. Dielectric coatings can also be used as anti-reflection or reflection coatings. To deposit $Si3N4$, we used silane (2%SiH4+98%N2) and ammonia ($NH3$) gases at 250 °C at a deposition rate of 140 A/min.

Lift-off

After metalization, the sample is left in acetone. Acetone dissolves the photoresist and the metal deposited on it will be lifted off and only the metal on the open area of the resist will remain on the sample surface. In order to get a good lift-off, we should wait a few hours and if the lift- off is not complete we should spray the sample with acetone. In the case of thick metallization (> 1micron) we may need ultrasound application, however this is a bit risky it may remove the metal which should stay on the sample surface. Therefore ultrasound must be applied in short time duration for instance a few seconds.

Chapter 4

Research on GaN/$Al_xGa_{1-x}N$

In this chapter, the work on the GaN/AlGaN based Schottky, p-i-n, and avalanche type photodetectors will be presented. Details of their designs, fabrication and the measurement results will be demonstrated.

4.1 Schottky Contact Photodetector

AlGaN Schottky photodiodes do not suffer from p+ contact problems. High quality Schottky and n+ ohmic contacts on AlGaN layers can be formed using standard processes. In addition, the temporal pulse response of Schottky detectors is not degraded by minority carrier diffusion which makes them suitable for high-speed operation [24,25,26]. Using these properties, high performance solar-blind AlGaN Schottky photodiodes were reported by several research groups [27,28,29]. Recently, we have demonstrated solar-blind AlGaN Schottky photodiodes with low dark current and high detectivity performance [30]. The bandwidth of these detectors was below the GHz level [31]. In this study, we report low dark current solar-blind AlGaN Schottky photodiodes with improved leakage and bandwidth performance. Leakage current of a few fA and bandwidth-efficiency product of 2.9GHz was achieved with the fabricated solar-blind AlGaN Schottky detectors.

Fabrication

The solar-blind devices were fabricated on MOCVD grown $Al_{0.38}Ga_{0.62}N$/GaN heterostructures. The detector active region was an unintentionally doped 0.8

micron thick $Al_{0.38}Ga_{0.62}N$ absorption layer. For ohmic contacts, highly doped n+ GaN layer was utilized. Fabrication process of the AlGaN Schottky photodiodes was accomplished using a microwave compatible five mask-level standard semiconductor process. In sequence, ohmic contact formation, mesa isolation, Schottky contact formation, surface passivation, and interconnect metallization steps were completed. Etching process of AlGaN/GaN layers was done using a reactive ion etching (RIE) system. Ti/Al alloy was used as ohmic contact metal. Schottky contacts were formed with thin (100Angstrom) semitransparent Au films.

Measurements

The fabricated devices were characterized in terms of current–voltage (I–V), spectral responsivity, and temporal pulse response. All measurements were made on wafer at room temperature using a low-noise microwave probe station. I–V measurements were performed with a high-resistance Keithley 6517A electrometer which featured a sub-fA current measurement resolution (Figure 4.1.1). However, mainly due to the pick-up noise from the environment and cables, the dark current measurements were limited by the 2 fA background current floor of the setup. Spectral responsivity measurements were done using a 175W xenon light-source, a monochromator, multi-mode UV fiber, lock-in amplifier and a calibrated Si-based optical power-meter. The UV-illuminated solar-blind detectors were biased with a DC voltage source, and the resulting photocurrent was measured using the lock-in amplifier. Temporal high frequency measurements were done at 267nm. Ultrafast UV pulses were generated using a laser set-up with two nonlinear crystals. A Coherent Mira 900F model femtosecond mode-locked Ti:sapphire laser was used to generate the pump beam at 800nm. The pump pulses were produced with 76MHz repetition rate and 140 fs pulse duration. These pulses were frequency doubled to generate a second harmonic beam at 400nm using a 0.5mm thick type-I b-BaB2O4 (BBO) crystal. The second harmonic beam and the remaining part of the pump beam were frequency summed to generate a third harmonic output beam at 267nm

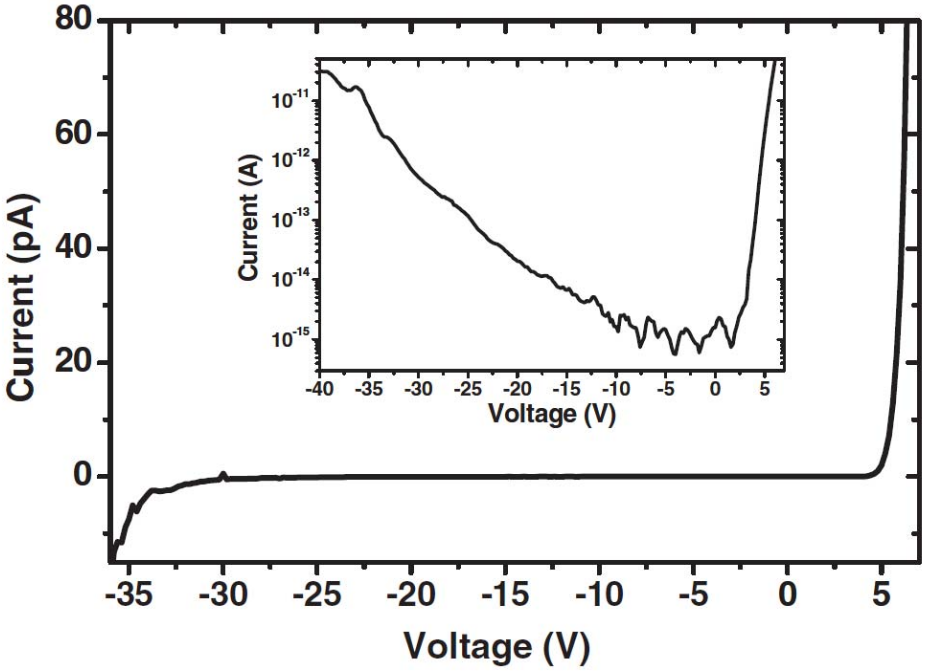

Figure 4.1.1 Dark current of a 30lm diameter solar-blind AlGaN photodiode.The inset shows the same plot in logarithmic scale.

using another type-IBBO crystal with thickness of 0.3mm. The resulting 267nm pulses had <1ps pulse-width and were focused onto the devices using UV enhanced mirrors and lenses. The detectors were biased using a DC voltage source and a 26GHz bias-tee. The resulting temporal pulse response was observed with a 20GHz sampling oscilloscope.

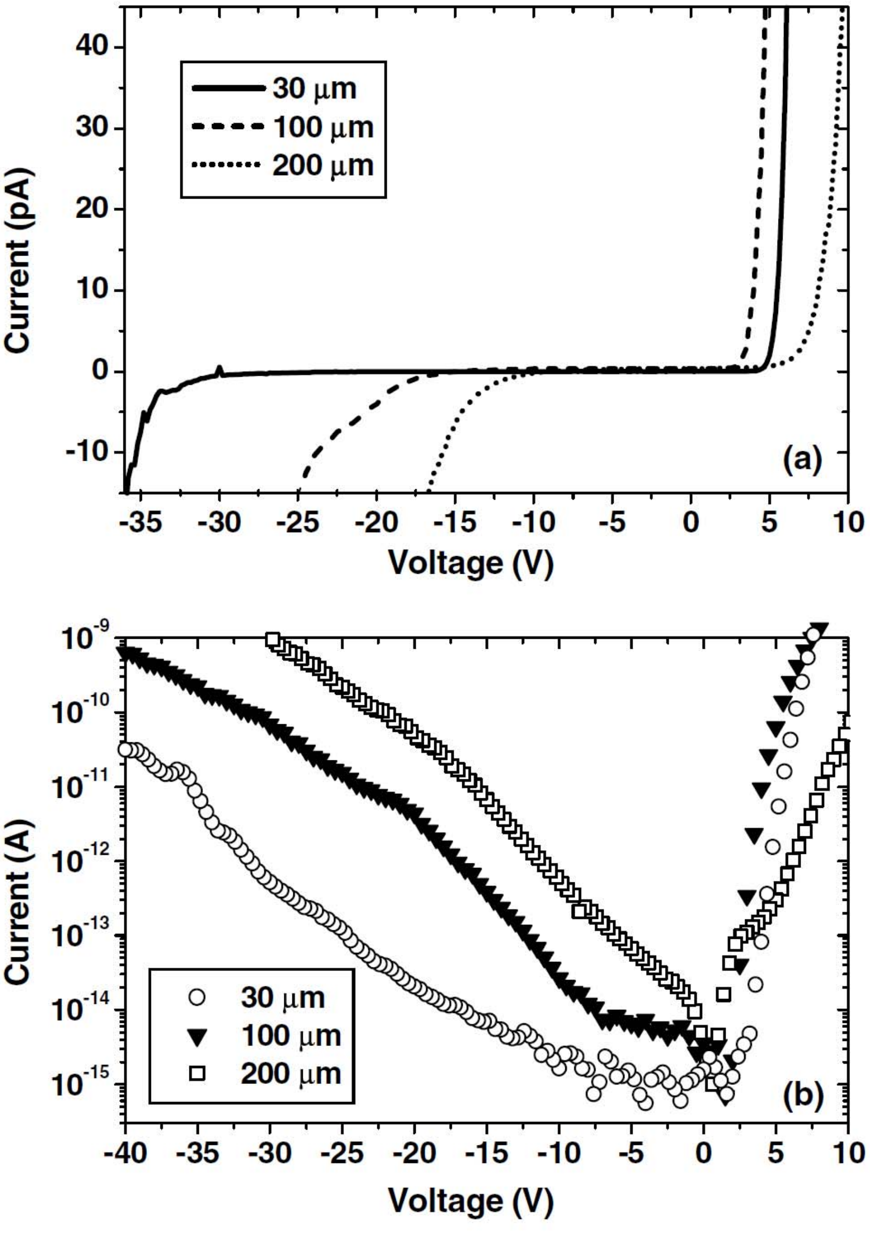

Figure 4.1.2 –V curves of AlGaN Schottky detectors with different device areas: (a) linear scale, (b) logarithmic scale.

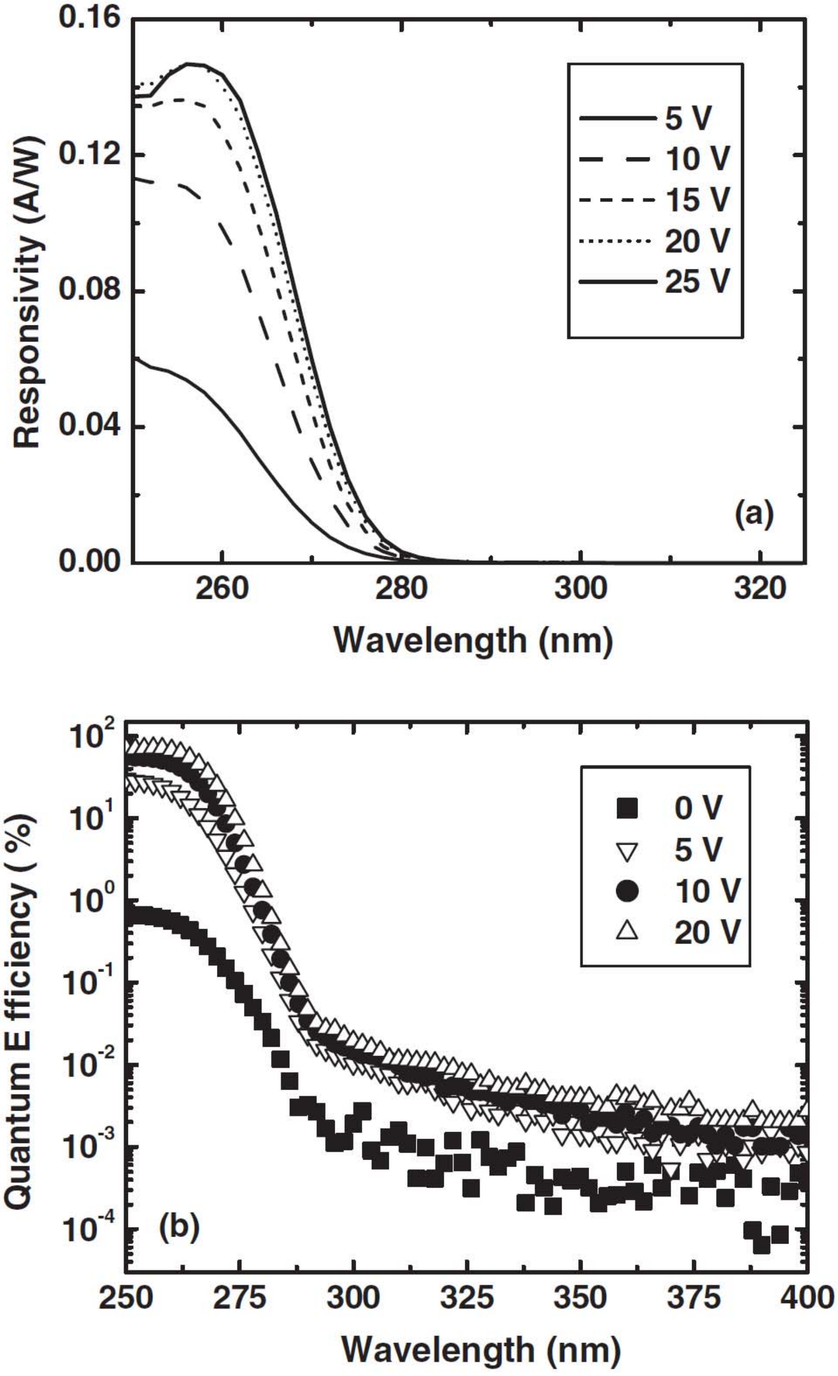

Figure 4.1.3 (a) Measured spectral responsivity curves as a function of reverse bias voltage, (b) corresponding spectral quantum efficiency of Schottky photodiodes.

Extremely low leakage currents were observed in the fabricated AlGaN Schottky photodiode samples. Fig. 4.1.1 shows the measured I–V curve of a small area (30lm diameter) device. The solar-blind device exhibited leakage current less than 3fA and 10fA for reverse bias up to 12V and 17V respectively. Under <12V reverse bias, the measured dark current fluctuated below the 3fA level due to the background noise of the setup. Sub-fA leakage currents were observed in this range. Using an exponential fit, we estimate the zero bias dark current less than 0.1 fA. The corresponding dark current density for this device at 12V was $4.2x10^{-10}$A/cm2. Typical reverse breakdown voltages were measured to be higher than 50V. In the forward bias regime, turn-on characteristic was observed at ~4V. Current in this regime increases with a much slower rate than in an ideal photodiode. At 10V bias, forward current was only 35nA. We attribute this result to the high series resistance of the devices. I–V measurements of larger area devices resulted in higher leakage currents. Fig. 4.1.2(a) and (b) show the dark I–V curves of 30µm, 100µm, and 200µm diameter devices in linear and logarithmic scale respectively. 200µm device displayed the largest dark current. We measured the reverse bias values where the devices displayed 1pA leakage current. For 30, 100, and 200 micro meter diameter detectors, 1pA dark current was reached at -32V, -18V, and -12V respectively. To make a fair leakage comparison between the devices, the current density values at 5V reverse bias were calculated.

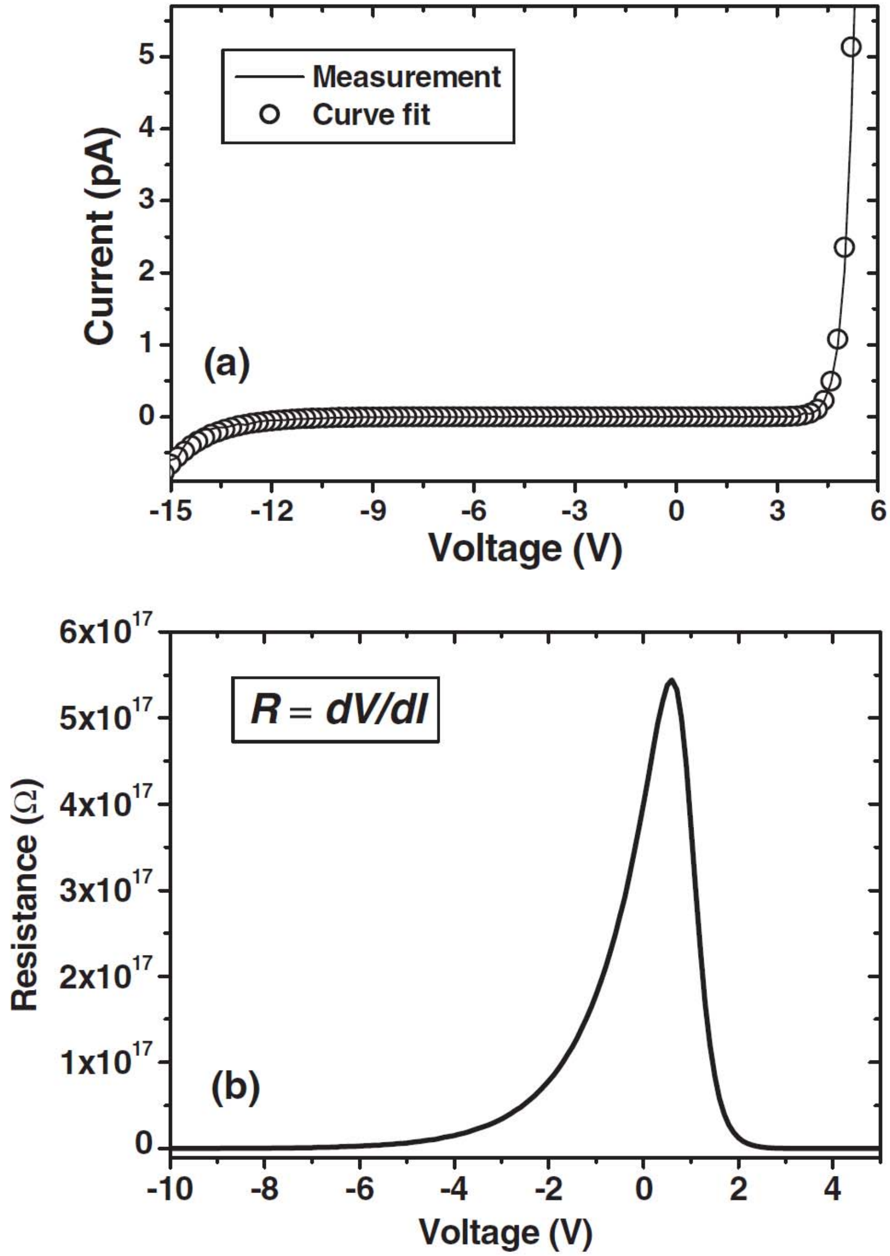

Figure 4.1.4 (a) Linear plot of I–V data and exponential fit for a 30lm diameter AlGaN detector, (b) calculated differential resistance for the same device.

100 µm and 200 µm devices exhibited 7fA and 67fA dark current at -5V, which leaded to 8.9 $\cdot$x10^{-11}A/cm^2 and 2.1x10^{-10}A/cm^2 dark current density values respectively. Due to the experimental setup limit, the actual dark current density

of 30 μm device at 5V reverse bias could only be estimated by exponential fitting curve as 3.3 x 10^{-11A}/cm2. These results correspond to the lowest leakage performance reported for AlGaN-based Schottky photodiodes. As expected, lower breakdown voltages were observed with increasing detector size. Turn-on voltages of -2.5V and -5V were measured for 100 μm and 200 μm devices respectively.

Spectral photoresponse of solar-blind AlGaN detectors was measured in the 250–400nm spectral range. The bias dependent measured spectral responsivity and quantum efficiency curves are plotted in Fig. 4.1.3.(a) shows the strong bias dependence of device responsivity. The peak reponsivity increased from 61mA/W at 250nm to 147mA/W at 256nm when applied reverse bias was increased from 5V to 20V. The device responsivity saturated for >20V reverse bias, which indicates the total depletion of undoped $Al_{0.38}Ga_{0.62}N$ absorption layer. A sharp decrease in responsivity was observed at ~265nm. The cut-off wavelength of the detectors was found as ~267nm, which ensured the true solar-blind operation of our detectors. Fig. 4.1.3(b) shows the semilog plot of the corresponding spectral quantum efficiency The photovoltaic (zero bias) quantum efficiency was very low. When the bias was increased to 5V, the efficiency was drastically improved by a factor more than 20. The low zero-bias efficiency value and strong bias dependent characteristic of device responsivity indicates photoconductive gain-assisted device operation. The observed photoconductive gain can be explained by the carrier trapping mechanism in Al0.38Ga0.62N active layer. Pulse response measurements have confirmed our suggestion with carrier trapping limited high-speed results. A maximum efficiency of 71% at 256nm was measured under 20V reverse bias. The visible rejection reached a maximum of ~4 x10^4 at 10V reverse bias. The detectivity performance of solar-blind detectors is thermally limited since the background radiation within the solar-blind spectrum is very low compared to thermal noise. Therefore, detectivity of solar-blind detectors can be expressed by $D^* \cong R_\lambda \sqrt{\frac{R_o A}{4kT}}$ where R_λ

is the zero bias reponsivity, R_0 is the dark impedance (differential resistance) at zero bias, and A is the detector area [32]. Curve fitting method was used to determine the differential resistance of the solar-blind devices [33]. Fig. 4.1.4 (a) shows the measured and exponentially fitted I–V curves for a 30µm diameter device. A good fit to the experimental data for reverse bias less than 15V was achieved. The differential resistance was calculated by taking the derivative (dV/dI) of the resulting curve, which is shown in Fig. 4.1.4.(b). The extremely low sub-fA dark currents resulted in very high resistance values. A maximum resistance of $5.44\text{x}10^{17}\Omega$ was obtained at 0.6 V. Zero-bias differential resistance, R_0 was slightly lower: $4.01 \text{ x } 10^{17}\ \Omega$. These resistance values are ~2 orders higher than previously reported solar-blind AlGaN detectors. Combining with $R\lambda = 1.4\text{mA/W}$, $A = 7.07 \text{ x}10^{-6}\text{cm}^2$, and T = 293K, we achieved a detectivity performance of $D^* = 1.83 \text{ x } 10^{13}\text{cmHz1/2W}^{-1}$ at 250nm. The detectivity was mainly limited by the low photovoltaic (zero bias) responsivity of the device.

Time-domain pulse response measurements at 267nm of the fabricated solar-blind Schottky photodiodes resulted in fast pulse responses with high 3-dB bandwidths. Bias and device area dependence of high-speed performance was analyzed. The corresponding frequency response of the temporal response was calculated using fast Fourier transform (FFT). The detector pulse response was bias dependent. Fig. 4.1.5(a) shows the pulse response of a 30 µm diameter Schottky photodiode as a function of applied reverse bias. Faster pulses with higher pulse amplitudes were obtained with increasing reverse bias as the n-AlGaN absorption layer was fully depleted under high reverse bias voltages. The pulsewidth decreased from 80ps to 53ps as bias was changed from 5V to 25V. The drop in full-width-at-half-maximum (FWHM) was mainly caused by the decrease in fall time. Short rise times of ~26ps were measured. Rise time did not change significantly with bias since it was close to the measurement limit of the 20GHz scope. The corresponding FFT curves are plotted in Fig. 4.1.5(b). As expected, 3-dB bandwidth values increased with reverse bias. A maximum 3-dB bandwidth of 4.1GHz was achieved at 25V. Table 1 summarizes the bias dependent high-speed measurement results. Fig.4.1.6(a) shows the normalized pulse responses displayed by detectors with different device areas. All measurements were taken under 25V reverse bias. Larger device area resulted in slower pulse response, which can be explained by the increased RC time constant. The corresponding frequency response curves are shown in Figure 4.1 6(b). 3-dB bandwidth dropped to 0.95GHz for 100lm diameter device. The device area dependent high-speed measurement results are given in Table 2. Mainly three speed limitations exist for photodiodes fabricated on defect-free materials: transit time across the depletion region, RC time constant, and diffusion of photogenerated carriers in low-field regions. The fabricated AlGaN Schottky detectors do not suffer from carrier diffusion. Moreover, the carrier transit times in AlGaN are much shorter than the measured response times due to the high carrier drift velocity [34,35,36]. The only limitation comes from RC time constant. This makes sense since the series resistance of these devices was high. If RC time constant was the only limitation for our devices, we should be able to fit the fall time components with a simple exponential decay function. However, a reasonable exponential fit with a single time constant could not be achieved. Instead, responses were fitted well with second order exponential decay functions, i.e. with a sum of two exponential decay functions with two different time constants. This shows that another limitation factor exists in our devices. We believe that the additional and slower decay tail was originated by the carrier trapping effect [37]. Photo-generated carriers can be trapped at the defects/trapping-sites in the AlGaN active layer, which are formed during the crystal growth process. The slower portion of the decay tail is possibly formed by the late arrival of the released carriers which were trapped in these sites. Figure 4.1.7 shows the curve fittings of decay parts for 30 µm and 60 µm diameter detectors.

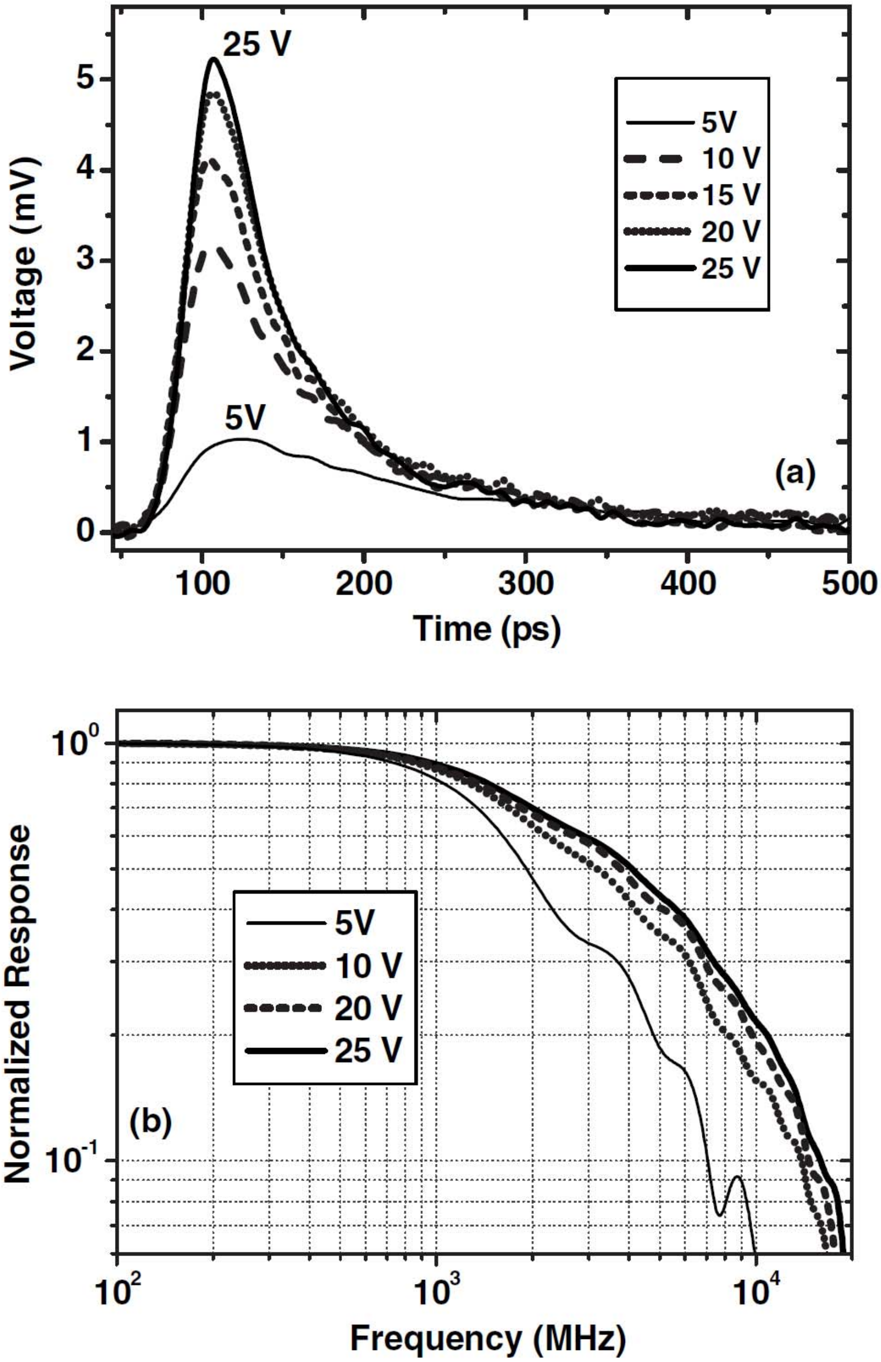

Figure 4.1.5 (a) High-speed pulse response of a 30lm diameter device as a function of applied reverse bias, (b) corresponding FFT curves of the temporal data.

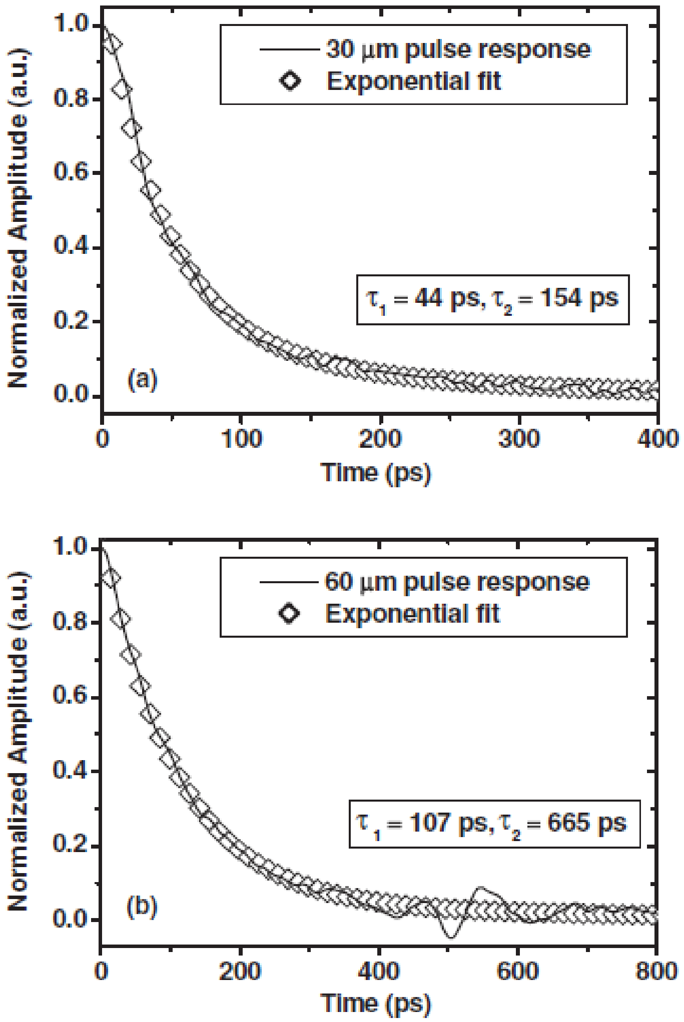

Figure 4.1.6 Second-order exponential fitting to the decay part of pulse response obtained with (a) 30lm diameter device, (b) 60lm diameter device.

Table 1
Bias dependent high-speed characteristics of AlGaN Schottky photodiodes

Bias (V)	Rise time (ps)	Fall time (ps)	FWHM (ps)	Bandwidth (GHz)
5	39	161	80	1.9
10	25	162	71	3.2
20	28	136	56	3.8
25	26	117	53	4.1

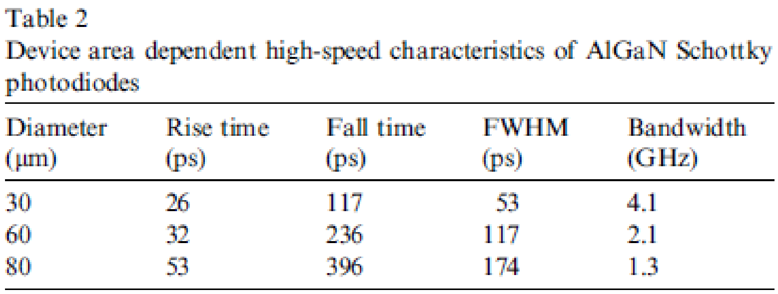

Table 2
Device area dependent high-speed characteristics of AlGaN Schottky photodiodes

Diameter (μm)	Rise time (ps)	Fall time (ps)	FWHM (ps)	Bandwidth (GHz)
30	26	117	53	4.1
60	32	236	117	2.1
80	53	396	174	1.3

Conclusions

In summary, high-performance solar-blind AlGaN Schottky photodiodes with low dark current, high responsivity, high detectivity, and high bandwidth were fabricated and tested. Setup limited 3fA dark current at 12V reverse bias was measured. Sub-fA leakage and 3.3 x10^{-11}A/cm^{2} dark current density was estimated at -5V. A maximum responsivity of 147mA/W at 256nm was measured at 20V reverse bias. Sub-fA dark current values resulted in record high differential resistance of R_0 = 4.01x10^{17} Ω. The solar-blind detectivity was calculated as D* = 1.8 x 10^{13} cmHz1/2W^{-1}at 250nm. Pulse response measurements resulted in GHz bandwidths. Combining the 3-dB bandwidth of 4.1GHz with 71% quantum efficiency, a bandwidth-efficiency performance of ~2.9GHz was achieved. This value corresponds to the highest bandwidth-efficiency performance reported for AlGaN-based solar-blind photodetectors.

4.2 P-I-N Photodetector

In this work, we present our experimental results on high performance GaN photodetectors. Our GaN photodetectors have higher breakdown voltage, lower current density, and higher responsivity when compared to the previously published GaN photodetector results in the literature. There are papers reporting maximum responsivity of 0.2 A/W at 355 nm for back illuminated GaN based *p-i-n* photodetectors which correspond to 70% quantum efficiency at zero bias [38], and 3-dB bandwidth of 1.6 GHz for *p-i-n* type photodetectors [39].

Fabrication

The GaN *p*-*i*-*n* structure used in the present study was grown on double-side polished *c*-plane sapphire (Al_2O_3) substrates by low-pressure metal organic chemical vapor deposition (MOCVD) system, which is located at the Bilkent University Nanotechnology Research Center. First, the wafer surface was cleaned by desorption in an H_2 environment at 1080 °C. Then, ~1000 Å AlN nucleation layer was grown at 500 °C by trimethylaluminum (TMAl) and ammonia (NH_3). The wafer surface was recrystallized by annealing at 970 °C. After recrystallization, a high temperature GaN buffer layer of 2500 Å was grown with trimethylgallium (TMGa) and high flow NH_3 at 1160 °C. A *n* layer with a thickness of 5000 Å was grown with silane (SiH_4), in turn, resulting in a carrier concentration of 10^{18} cm−3. The growth continued with a 5000 Å *i* layer. In the last step, an 800 Å *p* layer with Mg doping by biscyclopentadienylmagnesium (Cp2Mg) was grown [40,41]. In all of the steps, the carrier gas was H_2 and the chamber pressure was kept at 200 mbars.

The samples were fabricated by a six-step microwavecompatible fabrication process [42] in class-100 clean room environment. The dry etching was accomplished by reactive ion etching (RIE) under CCl_2F_2 plasma, 20 SCCM (SCCM denotes cubic centimeter per minute at STP) gas flow rate, and 200 W rf power conditions. Mesa structures of the devices were formed via the RIE process by etching all of the layers ~1.2 µm down to the nucleation layer for mesa isolation. After an Ohmic etch of ~0.74 µm, Ti/Al (100 Å/1000 Å) contacts and Ni/Au (100 Å/1000 Å) contacts were deposited by thermal evaporation and left in acetone for the lift-off process. The Ohmic contacts were annealed at 750 °C for 45 s. Thereafter, a 300 nm thick Si3N4 was deposited via plasma enhanced chemical vapor deposition for passivation. Finally, an ~0.4 µm thick Ti/Au interconnect metal was deposited and lifted-off in order to connect the *n*-type and *p*-type Ohmic contact layers to the coplanar waveguide transmission line pads.

Measurments

For the present study, current-voltage (*IV*), quantum efficiency (QE), capacitance-voltage (*CV*), and high speed measurements were performed. *IV* characterization of the fabricated photodetectors was carried out by using a Keithley 6517A high resistance electrometer with low noise triax cables. QE measurements were performed using a xenon arc lamp, monochromator, UV-enhanced fiber, and SRS lock-in amplifier. The capacitances of diodes were measured by an Agilent 4980A *LCR* meter. The consistency of the measured current levels, in the dark and illuminated cases, was confirmed by all the three current measurement made by these different experimental setups.

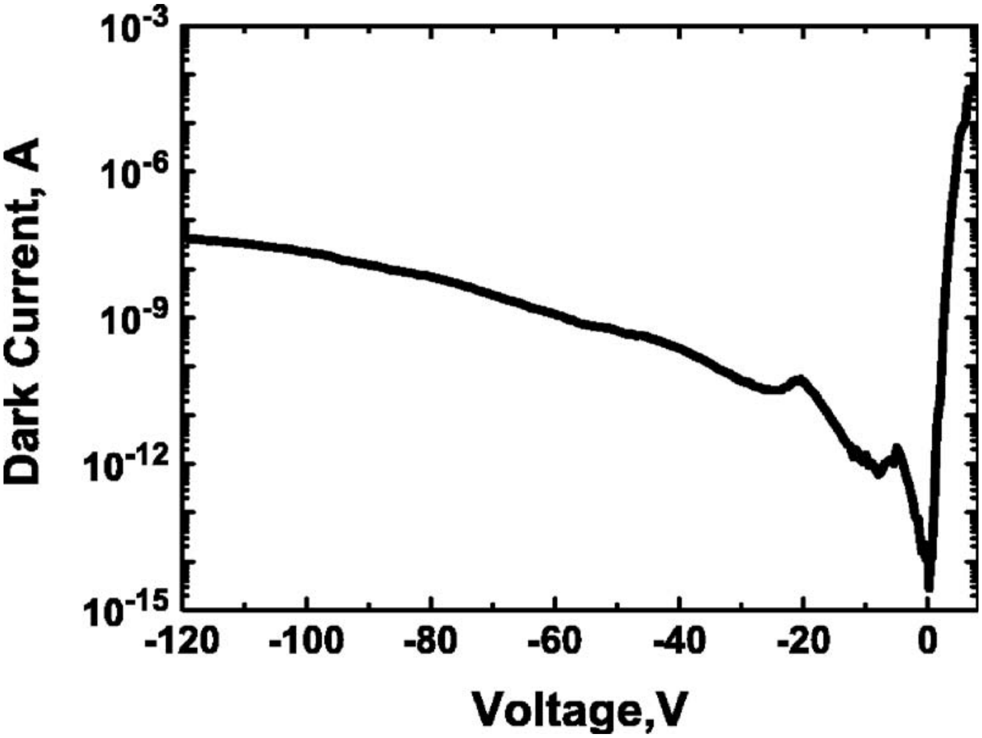

Figure 4.2.1 Current voltage measurements of a photodetector with a 200 µm diameter.

The *IV* measurement results in Fig. 4.2.1 show that the zero bias dark current of a 200 µm diameter photodetector was 14 fA, and with corresponding current density of 44 pA/cm2. This current level corresponds to the background noise floor of the electrometer used for the experiments. At 1 V reverse bias, the dark current of the device was 20 fA and at 5 V it was 1.6 pA. The breakdown voltages of the photodetectors were measured to be higher than 120 V.

The turn-on voltage of the fabricated device was around 3 V. The current level of the device for biases below 0.2 V was below the measurement limit. Therefore, a linear fit to the *IV* curve of the device was made for bias values from 0.2 to 0.7 V. Using this linear fit, the ideality factor of the photodiode was calculated as n=1.97. The contact resistances were 0.75 kΩ for *n*-type contacts and 15.0 kΩ for *p*-contacts with 100x200 μm^2 contact pads.

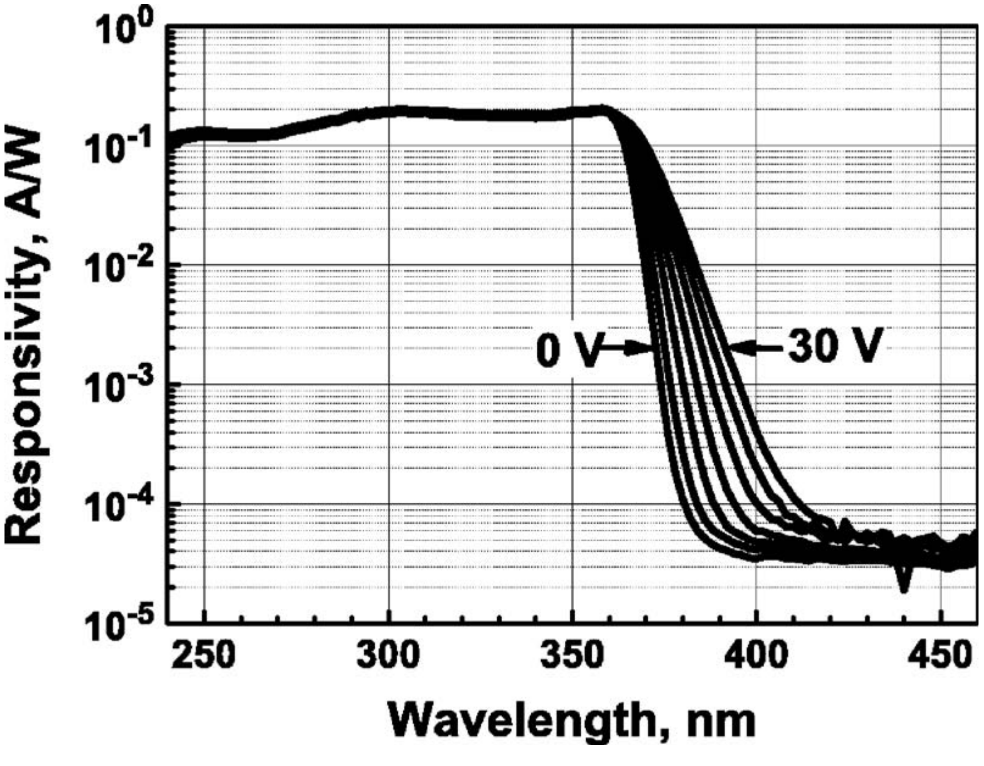

Figure 4.2.2 Responsivity of a 100 µm diameter photodetector for different reverse bias voltages.

We measured responsivity of 100 _m diameter diodes for bias voltages up to 30 V and observed a maximum UV/visible rejection ratio of 6.7x10^3 for wavelengths longer than 400 nm (Fig. 4.2.2). Responsivity at 358 nm was 0.20, which corresponds to 70% quantum efficiency. For wavelengths below 360 nm, the responsivity of the devices did not significantly change with applied reverse bias voltages larger than 5 V. Apparently, the diodes were depleted for small voltages, and in order to confirm this effect we performed *CV* measurements of the fabricated devices.

Figure 4.2.3 shows the QE (at 358 nm) and the capacitance measurements of a 100 μm diameter device as a function of applied reverse bias. The QE quickly increased from 64% at 0 V reverse bias to 68% at 5 V reverse bias. For applied reverse biases larger than 5 V, the QE stayed almost constant with a maximum of 70% at 30 V applied reverse bias. The capacitance of the 100 μm diameter device also had a similar dependency on applied reverse bias. The capacitance quickly dropped from 3.86 pF at 0 V applied reverse bias to 3.7 pF at 5 V applied reverse bias. Afterwards, the capacitance of the device slowly decreased

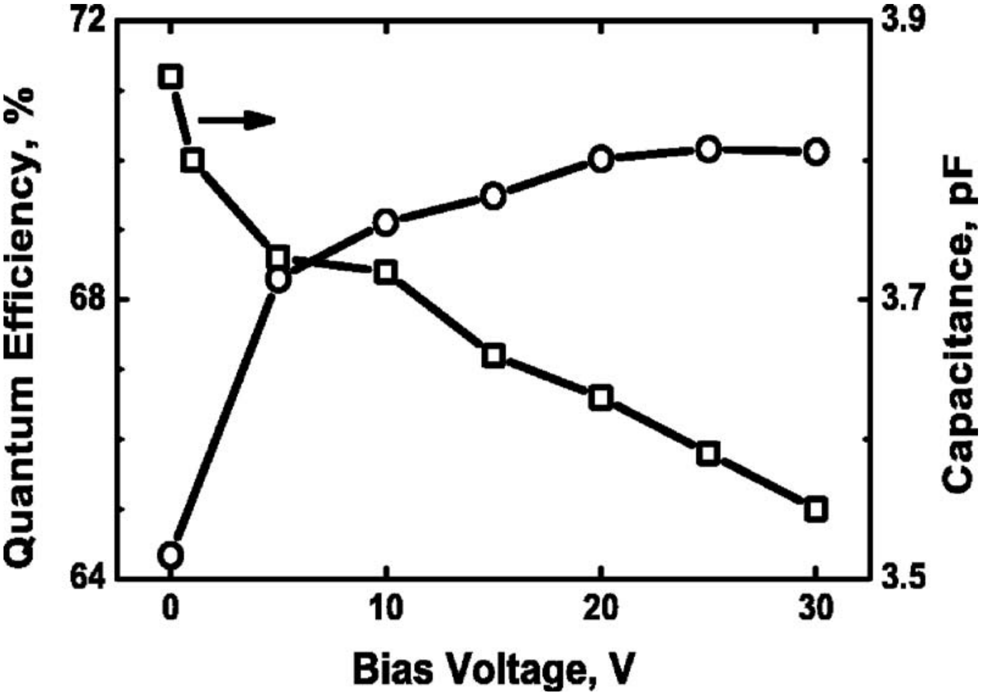

Figure 4.2.3 Voltage dependence of the quantum efficiency and capacitance for 100 μm diode.

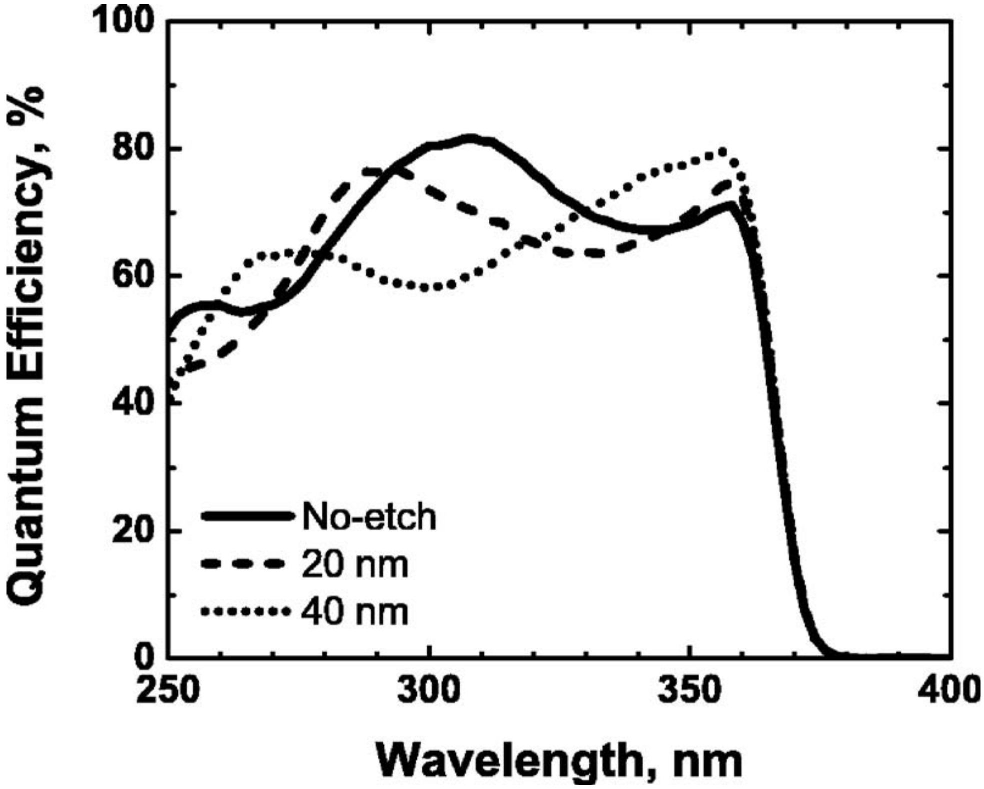

Figure 4.2.4 Spectral quantum efficiency of the photodetector after 0, 20, and 40 nm recess etch of the top dielectric film.

to 3.55 pF as the reverse bias voltage was changed to 30 V. These data clearly showed that most of the intrinsic region was already depleted at very low voltages.

Figure 4.2.4 shows that the peak QE of the fabricated device was at 300 nm under 5 V bias. This was in contradiction with the normally expected peak wavelength of 360 nm due to the band gap of GaN. This shift in peak QE wavelength can be explained with the additional optical phase coming from the finite thickness of the deposited dielectric layer. A similar shift was also observed in transfer matrix method (TMM) simulations of the QE for devices with varying top dielectric thicknesses. In order to confirm this explanation by experiments, the top Si3N4 layer was etched with diluted HF:H2O (3:500 ~ml) solution in 20 nm. Figure 4 shows the QE measurements after 0, 20, and 40 nm recess etch of the top dielectric film. After a total etch of 40 nm, the peak QE was measured to be 80.1%, while the peak responsivity was 0.23 A/W under 5

V bias at 356 nm. To our knowledge, the 0.23 A/W responsivity value corresponds to the highest responsivity for the front illuminated GaN based *p*-*i*-*n* photodetectors reported in the scientific literature.

Using an ultrafast mode-locked fiber laser module with output pulses at 266 nm and 10 ps FWHM (full width at half maximum), we performed the high speed measurement of fabricated *p*-*i*-*n* photodiodes. Figure 4.2.5 shows the temporal pulse response and the FFT (fast Fourier transform) of the *p*-*i*-*n* photodetectors. We measured 48 ps rise time, 351 ps fall time, and 109 ps FWHM from a 100 μm diameter device under 5 V reverse bias voltage. From the FFT data, the corresponding 3-dB bandwidth was found to be 1.16 GHz. This performance is close to the best 3-dB bandwidth of 1.6 GHz reported in the literature for GaN-based *p*-*i*-*n* photodetectors.

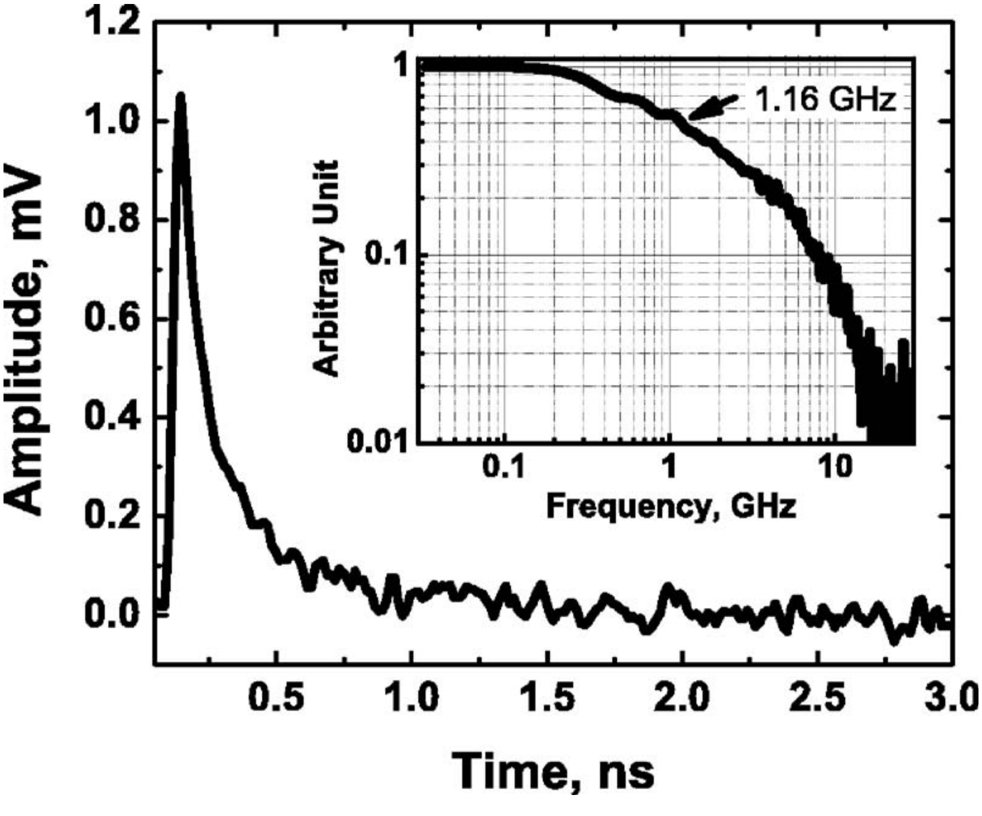

Figure 4.2.5 Temporal pulse response of the 100 μm micron diameter *p-i-n* photodiodes under 5 V reverse bias voltage and the corresponding frequency response (inset).

Conclusion

In conclusion, we presented the growth, fabrication, and characterization of high performance GaN-based *p*-*i*-*n* photodetectors. The optimized MOCVD growth conditions resulted in epitaxial samples that yielded high performance devices. A maximum 80.1% QE corresponding to 0.23 A/W responsivity at 356 nm, was achieved. The dark current of a 200 μm diameter circular diodes was measured to be 14 fA, along with a breakdown voltage larger than 120 V. To our knowledge, in terms of breakdown voltage, current density, and responsivity, the reported results are better than the previously published GaN photodetector results in the scientific literature.

Avalanche Photodetector

4.3 First Solar-blind AlGaN photodiode

The recent developments in GaN/AlGaN material growth technology have led to the fabrication of high performance photodetectors operating in the UV spectral region. AlGaN-based Schottky [43,44], p-i-n [45,46] and MSM [47] photodetectors with excellent detectivity performances have been reported. However, very few GaN-based avalanche photodiodes (APDs) were reported in the literature at the time this work is sent for publication [48,49,50,51,52,53], and there are not any publications reporting AlGaN-based APDs. The high defect densities in the epitaxial layers grown on lattice-mismatched substrates result in a premature microplasma breakdown before the electric field can reach the bulk avalanche breakdown level, which is a major problem for the AlGaN/GaN APDs. In this paper, we report the epitaxial growth, fabrication, and characterization of AlGaN-based APDs operating in the solar-blind spectral region.

Fabrication

The epitaxial structure of the front-illumination Schottky detector wafer was designed to achieve true-solar blindness, very low dark current, high solar rejection, and high breakdown. Low leakage and high breakdown are needed in order to see the avalanche effect. The Al0.38Ga0.62N absorption layer was used to achieve $\lambda c<280$ nm. The Al*x*Ga1−*x*N/GaN epitaxial layers of our heterojunction Schottky photodiode wafer were grown on a 2 in. single-side polished (0001) sapphire substrate using the Aixtron 200/4 RF-S MOCVD system located at the Bilkent University Nanotechnology Research Center. A thin AlN nucleation layer and a subsequent 0.5 µm thick unintentionally doped GaN mesa isolation layer was first grown. This was followed by the growth of a highly doped (n+=2x10^{18} cm^{-3}) 0.6 µm thick GaN Ohmic contact layer and a 0.2 µm thick Al0.38Ga0.62N layer at the same doping level. The epitaxial growth of the wafer was completed with the deposition of a 0.8 µm thick undoped Al0.38Ga0.62N active layer. The highly doped GaN layer was used for the Ohmic contact region due to the difficulty of obtaining high-quality Ohmic contacts with Al*x*Ga1−*x*N layers. The *n*-type doped 0.2 µm thick Al0.38Ga0.62N layer was used as a diffusion barrier for the photocarriers generated in the GaN Ohmic contact layer. Such a diffusion barrier is expected to increase the solar-blind/near-UV rejection ratio of the detector.

The samples were fabricated by using a five-step microwave-compatible fabrication process in a class-100 clean room environment. First, the Ohmic contact regions were defined via reactive ion etching (RIE) under CCl_2F_2 plasma, a 20 sccm gas flow rate, and 100W rf power. The etch rates for the GaN and Al0.38Ga0.62N layers were 326 and 178 Å/ min., respectively. After an Ohmic etch of ~1.2 µm,Ti/Al (100 Å/1000 Å0 contacts were deposited via thermal evaporation and left in an acetone solution for the lift-off process. The contacts were annealed at 650 °C for 60 s in a rapid thermal annealing system. A ~100 Å thick Au film was evaporated in order to form Au/AlGaN Schottky contacts. Mesa structures of the devices were formed via the same RIE process, by etching all of the layers ~2.1µm down to the sapphire substrate layer for better mesa isolation. Then, a 200 nm thick Si3N4 was deposited via plasmaenhanced chemical vapor deposition (PECVD) for passivation. Finally, a ~0.6 µm thick Ti/Au interconnect metal was deposited and lifted off to connect the Schottky layers to the coplanar waveguide transmission line pads.

Measurements

Figure 4.3.2(a) shows the current-voltage characteristics of a device with a 100 µm diameter. The device showed almost unity-gain behavior for voltages between 10 and 50 V, and the photocurrent was approximately 10 nA. After 50 V, avalanche gain has been observed from the device. As shown in Fig. 4.3.2(b), the maximum reproducible avalanche gain was 25 at 72 V reverse bias. The onset avalanche gain field was estimated to be approximately 1 MV/cm. Although we had observed avalanche gains as high as 200 (at ~85 V reverse bias) from some of the devices, the performance of these devices degraded rapidly after the measurements.

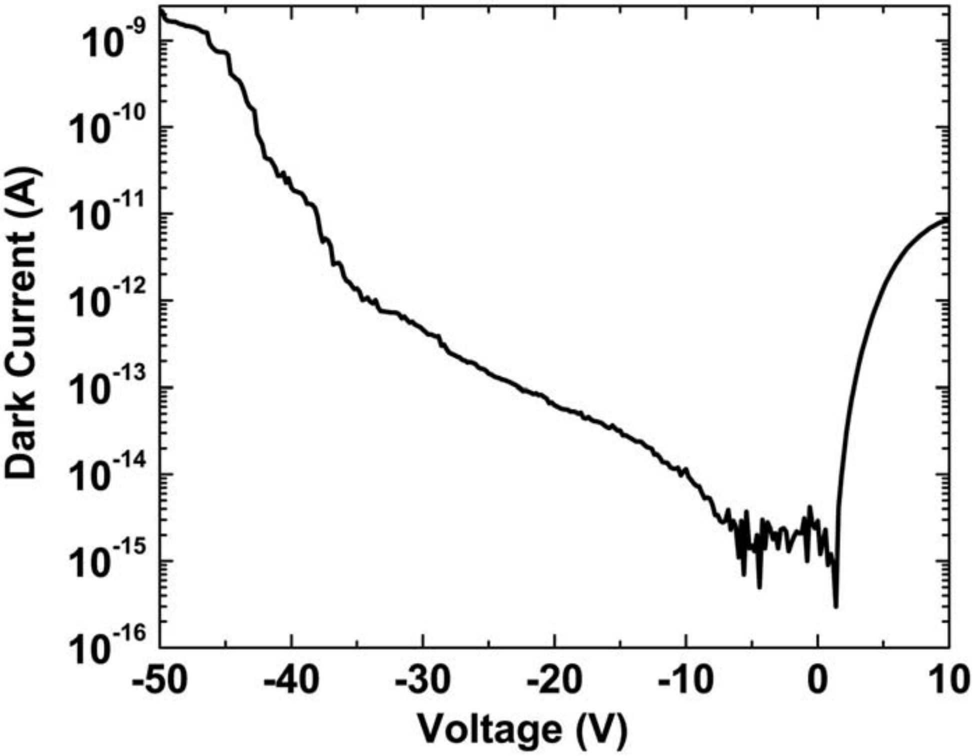

Figure 4.3.1 Dark current of a 60 µm diameter photodetector.

Figure 4.3.3(a) shows the quantum efficiency measurements of a 100 μm diameter device for different bias voltages. Under a 25 V reverse bias voltage, the device had a maximum quantum efficiency of 55% at 254 nm. The cut off wavelength was ~270 nm for all measurements. Figure 4.3.3(b) shows the responsivity measurements of the same photodetector. The peak responsivity was 0.11 A/W at a wavelength of 254 nm. The device had a rejection ratio of more than four orders of magnitude with wavelengths larger than 362 nm at a 25 V reverse bias. Using the thermal-noise-limited detectivity (D^*) formula, where R_λ is the device responsivity at zero bias, R_0 is the zero volt dark impedance, and A is the detector area, D^* is found as 4.68 $\times 10^{13}$ cm Hz1/2 /W, which is higher than our earlier results[54]. The corresponding noise-equivalent power (NEP) is 1.89 x10−16 W/$\text{Hz}^{1/2}$.

Finally, the noise characterization of the solar-blind detectors was carried out using a fast Fourier transform spectrum analyzer, current amplifier, dc voltage source, and a microwave probe station. In the 1 Hz–10 kHz range, our low-leakage, high breakdown voltage solar-blind photodetectors had noise power densities below the resolution level of the instrument. Even under 30 V, the detector noise did not exceed the measurement setup noise floor of 3 $\times 10^{-29}$ A^2 /Hz at 10 kHz. Therefore, we measured devices with higher leakage currents in order to observe the bias dependence of the spectral noise density. We took a 100 μm diameter device that has higher dark current (5×10^{-7} A at 35 V) and a lower breakdown voltage near 50 V. As can be seen in Fig. 4.3.4, $1/f$ (flicker) noise is the dominant noise mechanism in our detectors. $1/f$ noise is known to result from contamination and crystal imperfection. Up to 30 V reverse bias voltage, the noise power density is nearly the same. At a 0 V bias voltage and 10 Hz, $Sn(f)$ is ~9.8 $\times 10^{-21}$ A^2 /Hz, at 30 V bias it is only ~3×10^{-20} A^2 /Hz, and at 50 V it is ~1.4×10^{-16} A^2 /Hz. The noise curves obey the $Sn=S_0 / f^b$ relation. S_0 depends on current, which is why the noise increases with an applied bias voltage in low frequencies.

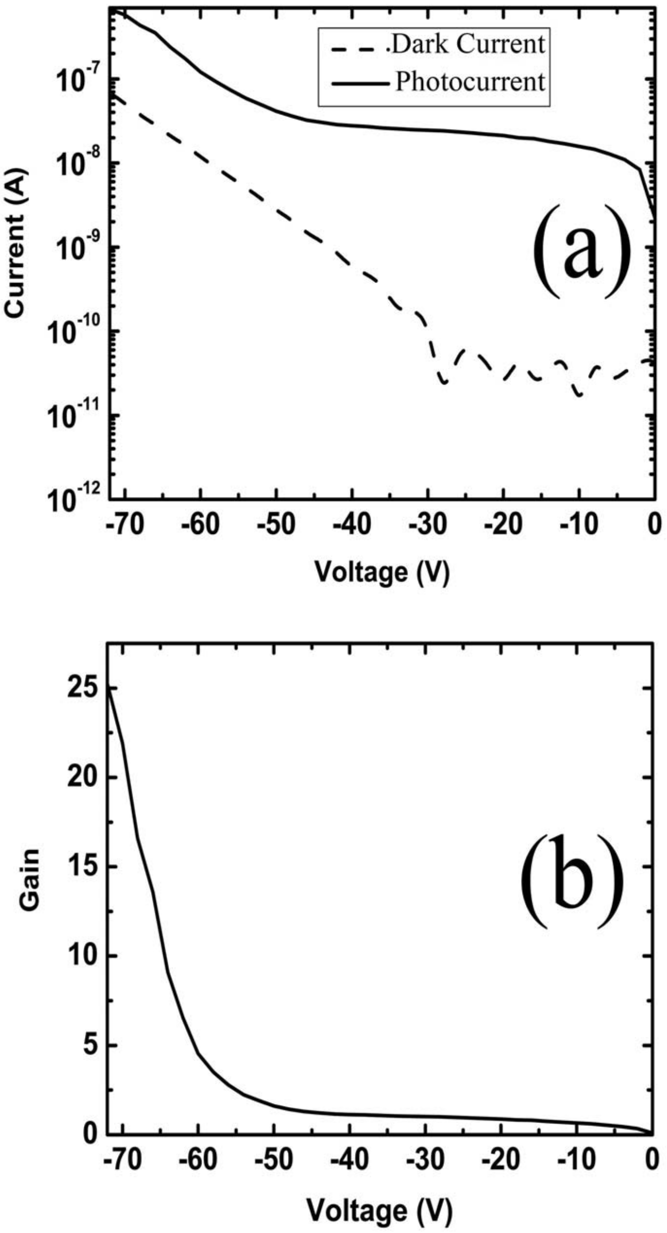

Figure 4.3.2 (a)Dark current and photocurrent measurement of a 100 micron diameter photodetector. (b) Corresponding avalanche gain of the same device.

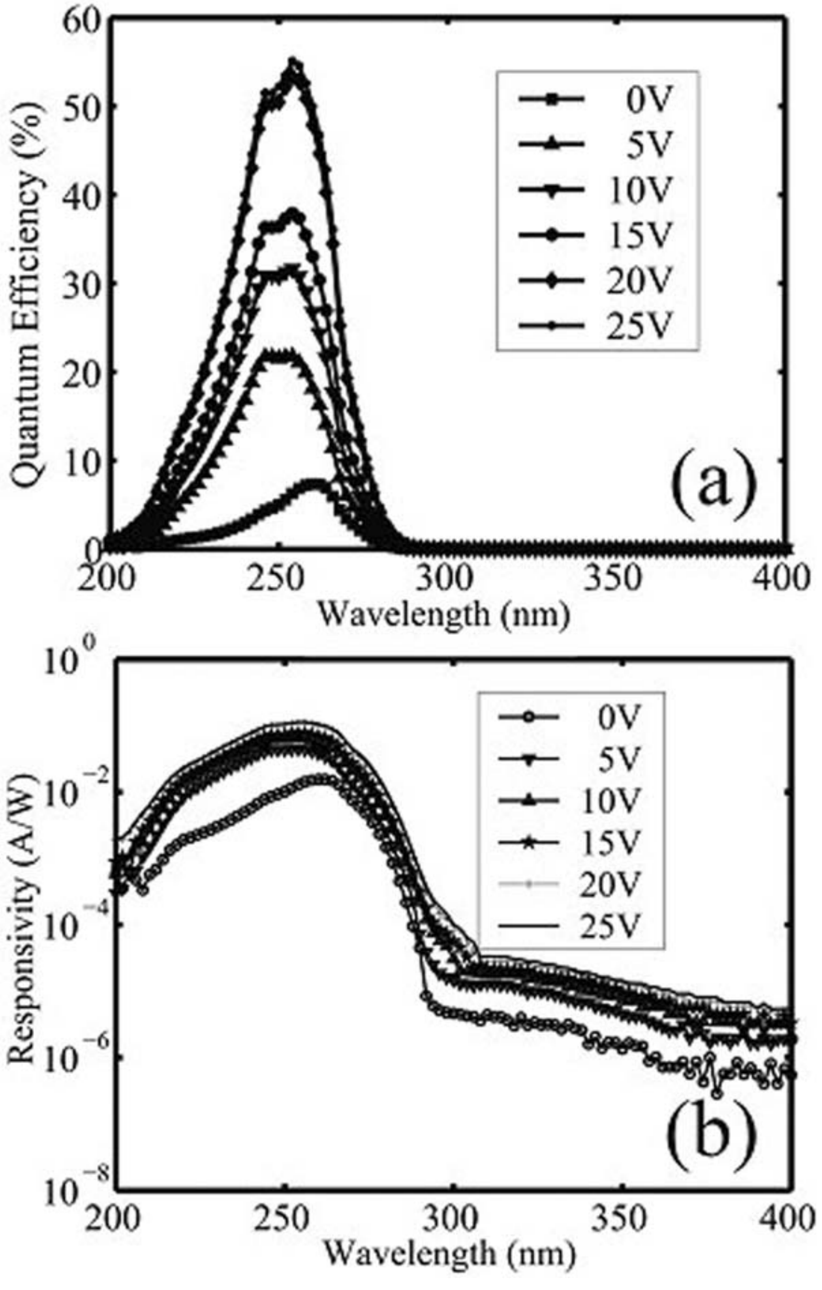

Figure 4.3.3 (a) Quantum efficiency measurements of a 100 µm diameter photodetector. (b) Responsivity measurement of the same device in a semilog scale.

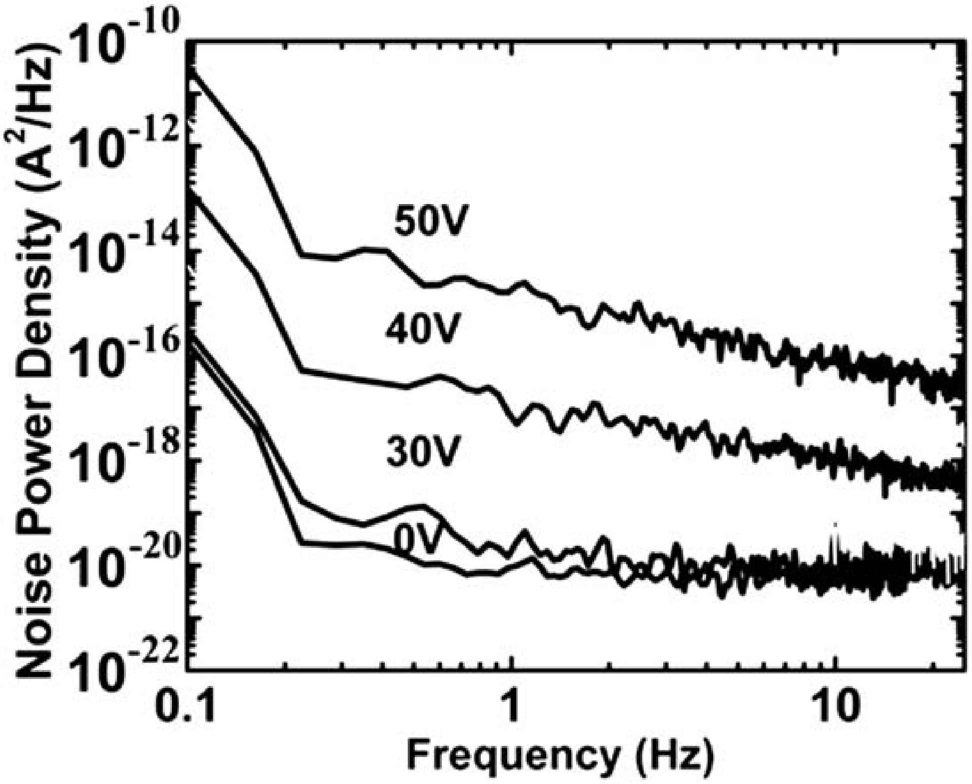

Figure 4.3.4 Spectral noise measurement of a high-leakage 100 μm diameter photodetector with a varying applied reverse bias.

Conclusion

In summary, we demonstared the first solar-blind AlGaN-based avalanche photodiodes with low dark current, low noise, and high detectivity reported in the literature. The photocurrent-voltage characteristics indicated a reproducible gain of ~25 at 72 V. The devices exhibited a maximum quantum efficiency of 55% and a peak responsivity of 0.11 A/W at a wavelength of 254 nm.

4.4 Experimental evaluation of impact ionization coefficients in AlGaN-based avalanche photodiodes

In order to design a good GaN/AlGaN based APD, it is essential to know the electron and hole impact ionization coefficients over a wide range of E fields. In the literature, there are theoretical works that report the impact ionization (II)

coefficients in GaN/AlGaN [55,56,57], and only one experimental work reports the evaluation of II coefficients in GaN [58]. However, there is no reported experimental work on the evaluation of II coefficients in AlGaN. In this work, we evaluated the experimental values of the II coefficients in $Al_{0.4}Ga_{0.6}N$
APDs.

Fabrication

The epitaxial structure of the avalanche photodetector is designed for back and front illuminations. In order to observe the avalanche effect, devices with low leakage and high breakdown are needed. The $Al_{0.4}Ga_{0.6}N$ absorption layer was used as a multiplication layer with λc=276 nm. The $Al_xGa_{1-x}N$ epitaxial layers of our Schottky photodiode wafer were grown on a 2 in. double-side polished (0001) sapphire substrate using a metal-organic chemical vapor deposition (MOCVD) system that is located at Bilkent University Nanotechnology Research Center. A thin AlN nucleation layer was deposited first, and subsequently a 0.3 μm thick AlN buffer layer was deposited. Thereafter, a highly doped (n+=1.08x10^{18} cm^{-3}) 0.3 μm thick $Al_{0.4}Ga_{0.6}N$

Ohmic contact layer was deposited, followed by a 0.2 μm thick $Al_{0.4}Ga_{0.6}N$ Schottky contact active layer with a relatively low doping (n−=1.45x10^{17} cm^{-3}). The highly doped $Al_{0.4}Ga_{0.6}N$ layer was used for the Ohmic contact region in order to be compatible with the back illumination.

The samples were fabricated by using a five-step microwave-compatible fabrication process in a class-100 clean room environment. The dry etching was achieved via reactive ion etching (RIE) under CCl2F2 plasma, a 20 SCCM (SCCM denotes cubic centimeter per minute at STP) gas flow rate, and 200 W rf power. The etch rates for $Al_{0.4}Ga_{0.6}N$ layers were 200 Å/min. The first mesa structures of the devices were formed via a RIE process, by etching all of the layers (~0.8 μm) down to the sapphire layer for better isolation. After an Ohmic etch of ~0.3 μm, Ti/Al (100 Å/1000 Å) contacts were deposited via thermal evaporation and left in an acetone solution for the lift-off process.

The contacts were annealed at 700 °C for 60 s in a rapid thermal annealing system. The Schottky surface treatment was made with a diluted HCl solution. An ~100 Å thick Au film was evaporated in order to form Au/AlGaN Schottky contacts. Then, a 200 nm thick Si_3N_4 was deposited via plasma enhanced chemical vapor deposition for passivation. Finally, ~0.25 µm thick Ti/Au interconnect metal was deposited and lifted off to connect the Schottky layers to the coplanar waveguide transmission line pads.

Measurements

The resultant devices had breakdown voltages higher than 60 V. To obtain better isolation, we etched down to the sapphire substrate, which enabled us to obtain low leakage current. The dark current for a 40 µm diameter device at 60 V was on the order of 1 nA. Figure 4.4.1 shows the dark current measurement with a low-level (on the order of femtoamperes) measurement setup. For reverse bias values below 15 V, the measured dark current was limited by the experimental setup and was approximately a few femtoamperes. The low dark current values proved the high growth quality of the AlGaN wafer with low dislocation densities. Hall measurements of the MOCVD grown samples showed that the active AlGaN layer had a Si doping concentration Nd=1.45x10^{17} cm^{-3}. Meanwhile, the Ohmic AlGaN layer had a Si doping concentration Nd=1.08x10^{18} cm^{-3}. Schottky barrier height of the fabricated photodetectors was calculated as 0.96 V by using the forward bias *I-V* data measured with a Keithley electrometer. To calculate the electric fields and depletion widths in the diode, we used one sided abrupt junction approximation.

Figure 4.4.2 shows the quantum efficiency measurements of 150 µm diameter devices at 25 V. Under a 25 V reverse bias voltage, the device had a maximum quantum efficiency of 48% at 282 nm and of 10.64% at 290 nm with front and back illuminations, respectively. As can be seen in Fig. 4.4.2, the devices are responsive to photons with energies higher than 4.4 eV which qualified them to be solar blind. According to the quantum efficiency data, the photocurrent does not significantly increase after 20 V. Therefore, we set the unity gain at 20 V. We also had to adjust the light source intensity for front and back illuminated photomultiplication measurements. We used the Schottky barrier diode to achieve pure electron injection when illuminated on the Schottky metal side with photon energy higher than the Schottky barrier height (290 nm) and pure hole injection when illuminated on the sapphire side with energy higher than the band gap[59].

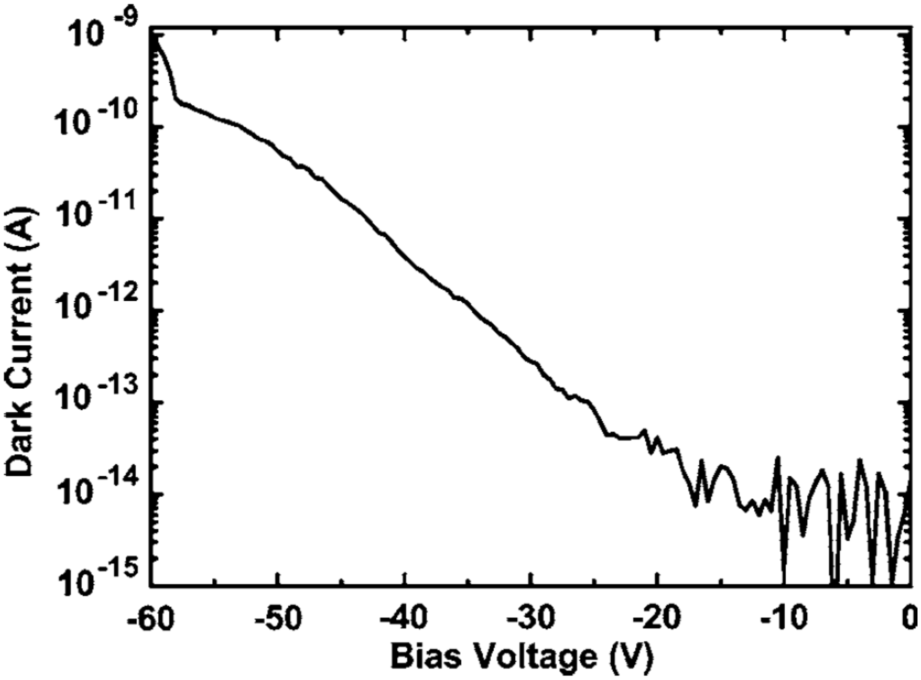

Figure 4.4.1 Dark current of a 40 µm diameter photodetector.

Figure 4.4.3 shows the reverse bias voltage dependence of the electron and hole multiplication factors, *Mn* and *Mp*. The multiplication factors are the ratios of the multiplied photocurrents to the primary photocurrents injected. The impact ionization coefficients (Fig. 4.4.4) can be found from the multiplication factor data using the following formulation [60,61,62]:

$$\beta(E_m)=\frac{2d}{W_0^2}\frac{1}{M_nM_p}\frac{dM_p}{dV}x\left(\alpha\left[E(d)\right]-\left\{\alpha\left[E(d)\right]-\beta\left[E(d)\right]\right\}\frac{1}{M_p}\right),$$

$$\alpha(E_m)=\frac{2d}{W_0^2}\frac{1}{M_n}\frac{dM_n}{dV}+\alpha\left[E(d)\right]M_p-\beta(E_m)\left(M_n-1\right),$$

$$W_0=\sqrt{\frac{2\varepsilon}{qN_d}},$$

$$E(x)=\frac{qN_d}{\varepsilon}(W-x),$$

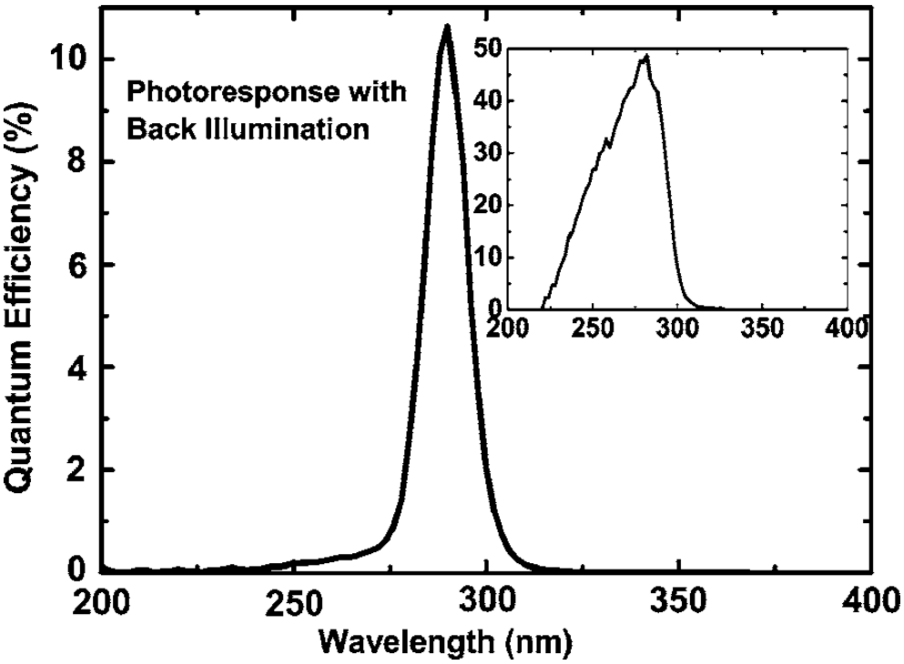

Figure 4.4.2 Quantum efficiency with back illumination, in which the inset shows the results for front illumination.

where *Em* is the electric field near the Schottky contact metal for a certain applied bias voltage, and *E*(*d*) is the electric field at the *n*−-*n*+ junction. *E*(*x*) is the electric field at depth *x* from the Schottky metal and *n*− layer interface, and *V* is the applied bias voltage across the device. Figure 4.4.4 shows the impact ionization coefficient data that were extracted from the multiplication factor data *Mn* and *Mp*. According to our calculations, alpha is larger than beta for the range of electric field 0.78<*E*<1.88 MV/cm. The ratio of alpha to beta decreases as the electric field increases. The impact ionization coefficients can be fitted into an exponential form,

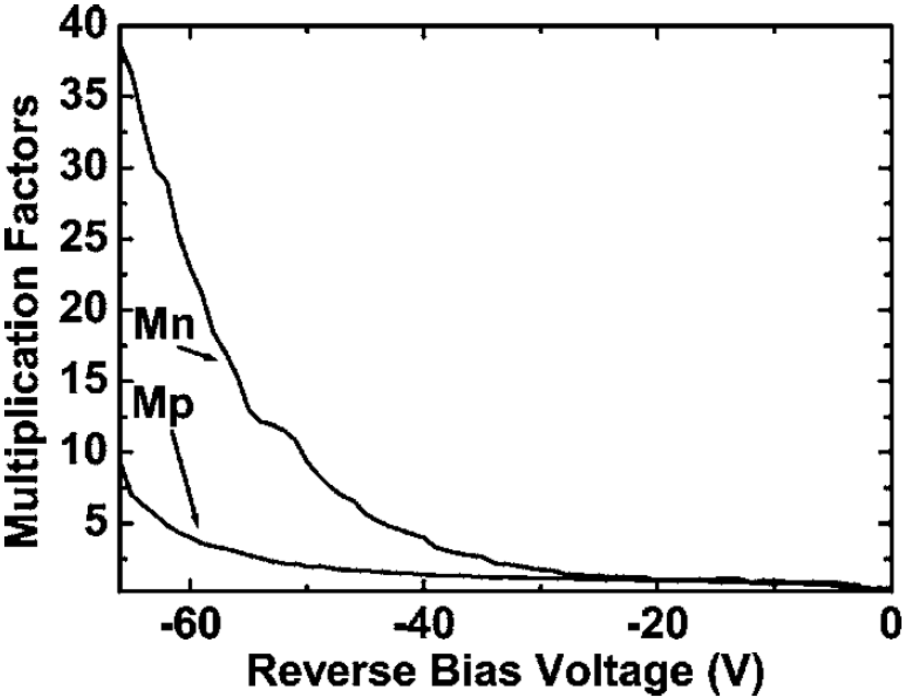

Figure 4.4.3 ***Mn*** **and** ***Mp*** **as a function of reverse bias voltage**

$$\alpha(E) = A_e \exp(-B_e / E)$$
$$\beta(E) = A_h \exp(-B_h / E)$$

$$\alpha(E) = A_e \exp(-B_e / E)$$

$$\beta(E) = A_h \exp(-B_h / E)$$

Where A_e=0.6x10^{6}cm^{-1}, B_e=3.6x10^{6}V/cm, A_h=3.4x10^{6}cm^{-1}, B_h=7.9x10^{6}V/cm. The theoretical electron impact ionization coefficients are significantly lower than our experimental impact ionization coefficients. We explain this discrepancy due to the lattice defects in the AlGaN layers (which cause microplasmas) and the nonuniform *E*-field distribution which were not considered in the theoretical simulations of [63].

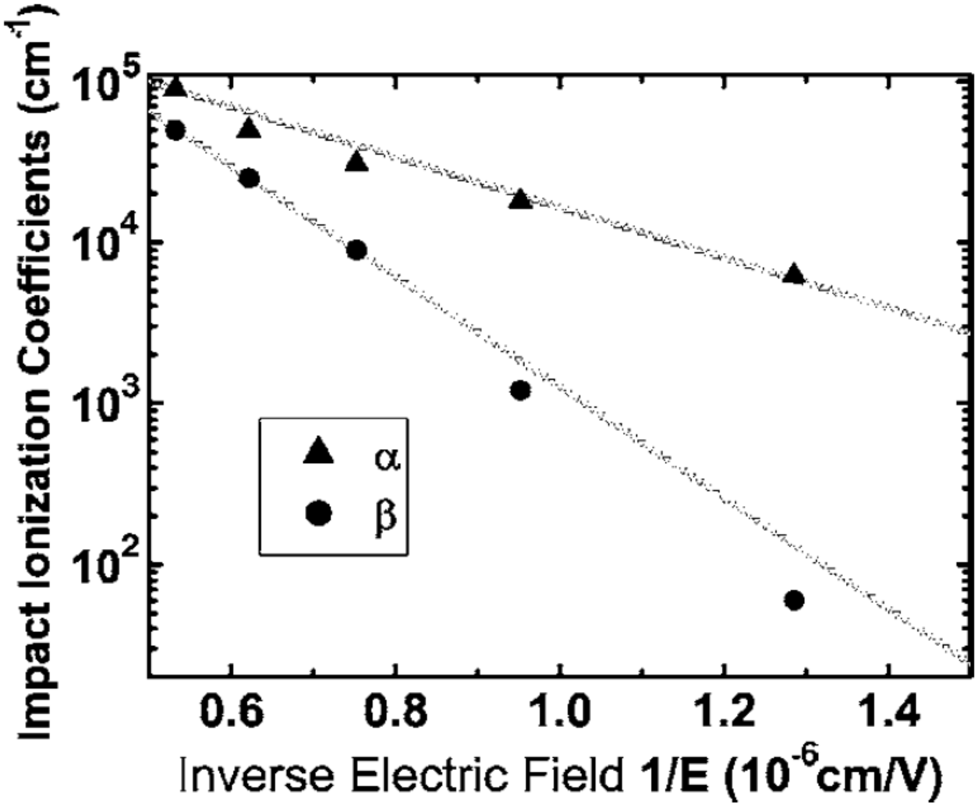

Figure 4.4.4 Electron and hole impact ionization coefficients in Al0.4Ga0.6N.

Conclusion

In summary, we present the MOCVD growth, fabrication, and characterization of AlGaN based solar-blind APDs. The impact ionization coefficients for electrons and holes were evaluated from the photomultiplication measurements. Over the electric field range, 0.77 MV/cm<*E* <1.88 MV/cm, alpha is found to be larger than beta.

4.5 Al$_x$Ga$_{1-x}$N-based avalanche photodiodes with high reproducible avalanche gain

The recent developments in high Al-content Al$_x$Ga$_{1-x}$N material growth technology made it possible to fabricate high performance solar-blind photodetectors operating in the ultraviolet (UV) spectral region with improved receiver sensitivity, low noise, low dark current density, and high speed [64,65,66]. AlGaN-based Schottky, *p*-*i*-*n*, and metal-semiconductor-metal photodetectors with very high performances have already been demonstrated [67,68]. The UV-filtering nature of the atmospheric ozone molecules blocks the solar radiation to reach the earth's surface for wavelengths shorter than 280 nm. In this case, UV photodetectors with cutoff wavelengths around 280 nm, which are also called solar-blind detectors, can detect very weak UV signals under intense background radiation. These devices have important applications including missile plume detection, chemical/ biological agent sensing, flame alarms, covert space-to-space and submarine communications, ozone-layer monitoring, and gas detection. Due to their high responsivity (600 A/W), high speed, high cathode gain (on the order of a million), and low dark current properties, photomultiplier tubes (PMTs) are frequently used in such applications. However, PMTs are very expensive and bulky. Besides, they require a cooling system, and they have high operation voltages in excess of 1000 V. To achieve solar-blind detection, PMTs should also be integrated with complex and expensive filters. In order to avoid these disadvantages, high performance solid-state UV photodetectors with high internal gain are needed [69]. Wide band-gap semiconductor photodetectors, such as Al$_x$Ga$_{1-x}$N with x=0.4, are ideal candidates for this purpose. These devices are intrinsically solar blind, in which no additional filters are needed, they have low noise [70], and fast response times [71]. The lack of high internal gain has been the major limitation for the usage of AlGaN photodetectors for applications that require high sensitivity detectors. There have been several theoretical research work that examined the avalanche effect in GaN and AlGaN-based structures [72,73,74]. Experimental work on both GaN and AlGaNbased avalanche photodiodes were also reported. However, reproducible high gain in AlGaN-based APDs is still a major limitation. In this work, we demonstrated the realization of solar-blind AlGaN-based avalanche photodetectors with reproducible high avalanche gain.

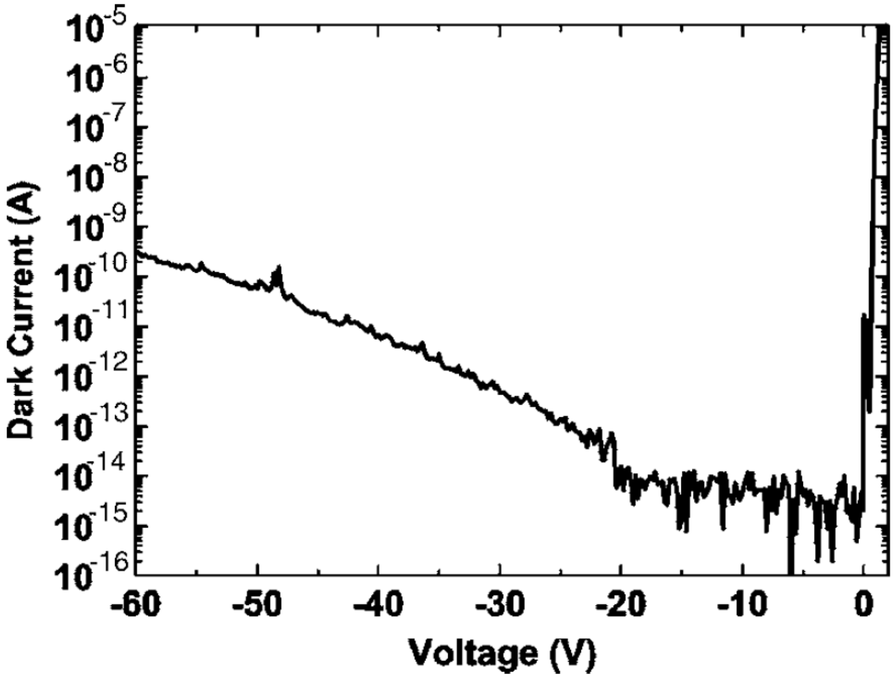

Figure 4.5.1 Dark current measurement data from a 40 µm diameter photodetector device.

Fabrication

The epitaxial structure of the avalanche photodetector is designed for solar-blind operation with high avalanche gain. The $Al_{0.4}Ga_{0.6}N$ absorption layer was used as a multiplication layer with λc=276 nm. The $Al_xGa_{1-x}N$ epitaxial layers of our Schottky photodiode wafer were grown on a 2 in. double side polished (0001) sapphire substrate using a metalorganic chemical vapor deposition (MOCVD) system, which is located at the Bilkent University Nanotechnology

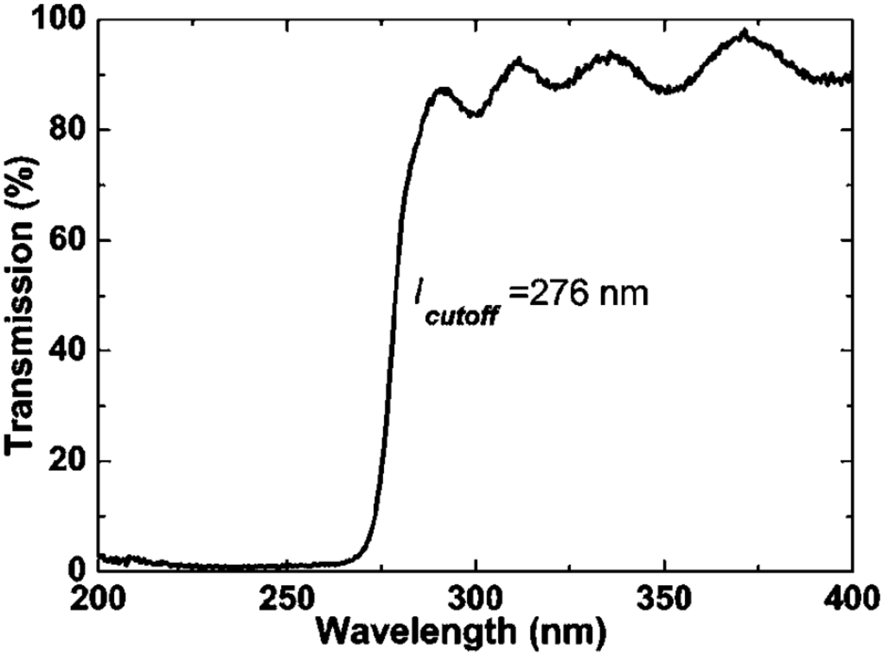

Figure 4.5.2 (a) Transmission data from a double side polished wafer which is used in the fabrication.

Research Center. First, a thin AlN nucleation layer was deposited, and then a 0.3 µm thick AlN buffer layer was deposited. Subsequently, a highly doped (*n*+=$1.08\text{x}10^{18}$ cm^{-3}) 0.3 µm thick Al0.4Ga0.6N layer was deposited for Ohmic contact, followed by a 0.2 µm thick Al0.4Ga0.6N layer with relatively low doping (n−=$1.45\text{x}10^{17}$ cm^{-3}) for Schottky contact.

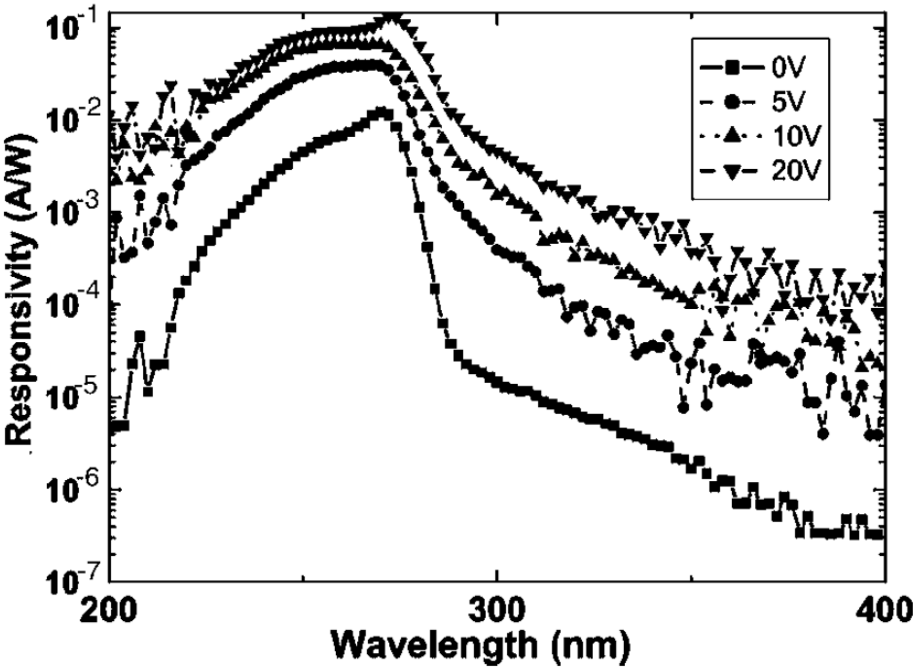

Figure 4.5.2.(b) Responsivity measurements result from a 150 μm diameter device.

The samples were fabricated by using a five-step microwave-compatible fabrication process in a class-100 clean room environment. The dry etching was accomplished via reactive ion etching (RIE) under CCl_2F_2 plasma, a 20 SCCM (SCCM denotes standard cubic centimeter per minute at STP) gas flow rate, and 200 W rf power. The mesa structures of the devices were formed via the RIE process, by etching all of the layers ~0.8 μm down to the sapphire layer for better mesa isolation. After an Ohmic etch of ~0.3 μm, Ti/Al (100 Å/1000 Å) contacts were deposited via thermal evaporation and left in acetone solution for the lift-off process. The contacts were annealed at 700 °C for 60 s in a rapid thermal annealing system. An ~100 Å thick Au metal was evaporated in order to form Au/AlGaN Schottky contacts. Thereafter, a 200 nm thick Si3N4 was deposited via plasma enhanced chemical vapor deposition for passivation. Finally, an ~0.25 μm thick Ti/Au interconnect metal was deposited and lifted-off to connect the Schottky layers to the coplanar waveguide transmission line pads.

Measurements

After fabrication, the devices were characterized in terms of current-voltage and spectral responsivity. The fabricated devices had breakdown voltages higher than 60 V. In order to have better mesa isolation, we etched down to the sapphire substrate, which enabled us to attain low leakage current. *I-V* measurements of the larger area devices resulted in higher leakage currents. Therefore, we chose to use the smaller area devices with 20, 40, and 60 _m diameters. Current-voltage characterization of the fabricated Schottky photodetectors was carried out by using a Keithley 6517A high resistance electrometer with low noise triax cables. Figure 4.5.1 shows the dark current measurements of a 40 µm diameter device. The dark current for a 40 µm diameter device at 60 V reverse bias was approximately 0.3 nA. For reverse bias values below 20 V, the measured dark current was limited by the experimental setup and was less than 8 fA. The Hall measurements of the MOCVD grown samples showed that the active AlGaN layer had a Si doping concentration $\mathrm{N}d=1.45\mathrm{x}10^{17}\ \mathrm{cm}^{-3}$ and the Ohmic AlGaN layer had a Si doping concentration $\mathrm{N}d=1.08\mathrm{x}10^{18}\ \mathrm{cm}^{-3}$.

Figure 4.5.2(a) shows the transmission characteristics of the as-grown epitaxial structure. The AlGaN layer absorbs all photons with energies higher than 4.4 eV. Figure 4.5.2(b) shows the responsivity measurements of a 150 µm diameter device. In parallel with the transmission measurement, the responsivity of the fabricated device has a sharp cutoff at 276 nm, which qualifies the AlGaN photodetectors to be solar blind. Under a 20 V reverse bias voltage, the device had a maximum responsivity of 0.13 A/W at 272 nm. Under 0 V bias, the device had a maximum responsivity of 12.2 mA/W at 270 nm under front illumination. The UV/visible rejection ratio for wavelengths larger than 350 nm is on the order of $2\mathrm{x}10^4$ under zero bias. Thermally limited detectivity is calculated as $D^*=1.4\mathrm{x}10^{14}\ \mathrm{cm\ Hz}^{1/2}\ \mathrm{W}^{-1}$ which corresponds to the highest value reported for an AlGaN-based Schottky photodiodes. Differential resistance at zero bias is

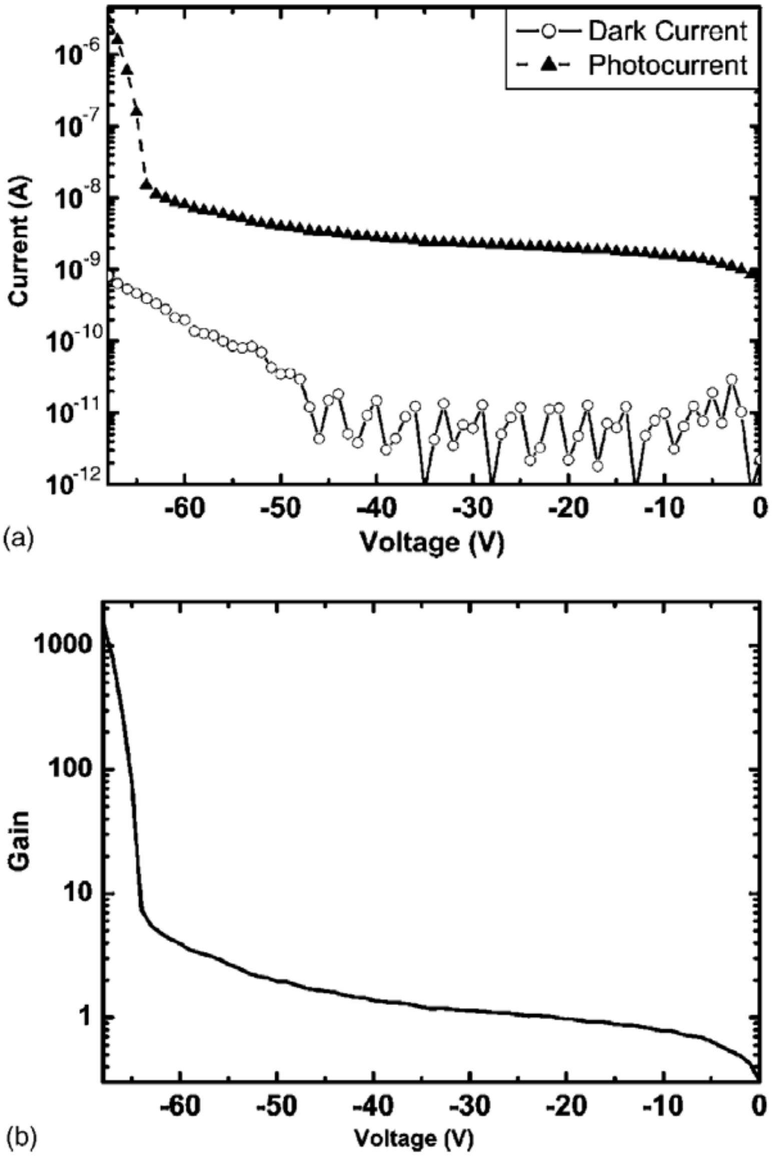

Figure 4.5.3 (a) Gain measurements for a 40 µm diameter device. (b) Avalanche gain extracted from the photocurrent measurements.

R_0=1.3x10^{16} Ω. According to the responsivity measurements, the photocurrent does not significantly increase after 20 V. Therefore, we set the unity gain at 20 V. From the photocurrent and dark current data, we calculated the avalanche gain by first taking the difference between the multiplied photocurrent and dark current data, and then normalizing it with respect to the unmultiplied difference of the photocurrent and dark current. The avalanche gain at a 68 V reverse bias was 1560, which is the highest reproducible avalanche gain reported in the literature for AlGaN-based solarblind APDs. We proved reproducibility by way of taking the dark current measurement after several photocurrent measurements, in which we saw no significant change in dark current (ten scans), and consequently, also none in the avalanche gain results (ten scans), which is shown in Figure 4.5.3.

We determined the voltage at which the unity gain occurs via *C*-*V* and lock-in assisted responsivity measurements. After the 20 V bias, the capacitance does not change which is an indicator of full depletion of the junction. Close to 20 V the lock-in assisted responsivity does not change considerably and after 20 V it does not increase steadily and significantly unlike avalanche gain which starts generally after 60V.

We also measured the dark currents under different temperatures. In Figure 4.5.4, the dark current of a photodetector shows a strong dependence on temperature. This result proves that Zener tunneling, which is a temperature insensitive process, is not a possible gain mechanism in these devices. The gain measurements showed an exponential dependence on voltage, in which we infer from this result that the photoconductive gain is not a possible gain mechanism in our devices. We know that the photoconductive gain increases linearly with voltage. Therefore, we conclude that the gain in these devices result from the avalanche multiplication of the photogenerated carriers in the active region of the devices.

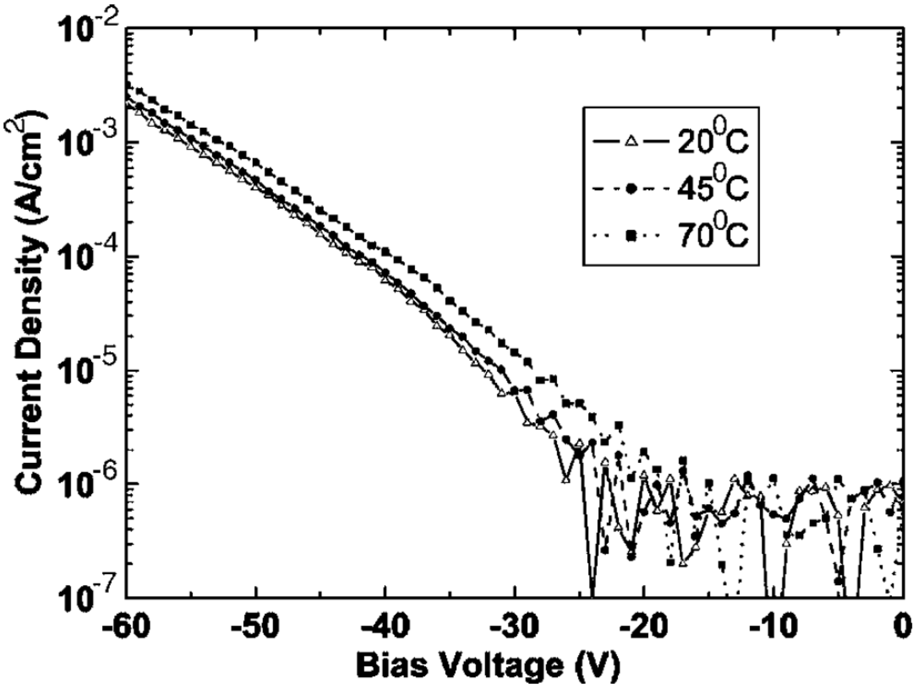

Figure 4.5.4 Dark current measurement data with varying temperatures.

Conclusions

In summary, we present the MOCVD growth, fabrication, and characterization of AlGaN-based solar-blind APDs. The avalanche gain at 68 V was in excess of 1560 with no Geiger mode breakdown. The electric field was on the order of 1.88 MV/cm. The gain in the active region of the devices is attributed to the avalanche multiplication of the photogenerated carriers. This work demonstrates the high potential of AlGaN APDs for replacement of the PMTs for high sensitive solar-blind photodetector applications.

Chapter 5

Conclusion and Suggestions for Further Research

In this thesis work, we have presented the design, fabrication, and characterization results from the GaN/AlGaN base UV photodetectors. During the growth the optical simulation results are also used as a guide for the efficient absorption in the active layer of the photodetector structure.

From the Schottky type photodiode, we have achieved the following results: The solar-blind detectors displayed extremely low dark current values: 30 μm diameter devices exhibited leakage current below 3fA under reverse bias up to 12V. True solar-blind operation was ensured with a sharp cut-off around 266nm. Peak responsivity of 147mA/W was measured at 256nm under 20V reverse bias. A visible rejection more than 4 orders of magnitude was achieved. The thermally-limited detectivity of the devices was calculated as 1.8x 10^{13}cmHz1/2W^{-1}. Temporal pulse response measurements of the solar-blind detectors resulted in fast pulses with high 3-dB bandwidths. The best devices had 53 ps pulse-width and 4.1GHz bandwidth. A bandwidth-efficiency product of 2.9GHz was achieved with the AlGaN Schottky photodiodes.

From the GaN based p-i-n type photodetector we have obtained the following results: The dark current of the 200 μm diameter devices was measured to be lower than 20 pA for bias voltages up to 5 V. The breakdown voltages were higher than 120 V. The responsivity of the photodetectors was ~0.23 A/W at 356 nm under 5 V bias. The ultraviolet-visible rejection ratio was 6.7x10^3 for wavelengths longer than 400 nm.

From the work on GaN/AlGaN based UV avalanche photodiodes, we have realized the first AlGaN based reproducible APD with avalanche gain higher than 25 at 72 V reverse bias.

We have evaluated the impact ionization coefficients of both electrons and holes for $Al_{0.4}Ga_{0.6}N$ material. A Schottky barrier, suitable for back and front illuminations, is used to determine the impact ionization coefficients of electrons and holes in an AlGaN based avalanche photodiode.

We also obtained high performance solar-blind photodetectors with reproducible avalanche gain as high as 1560 under ultraviolet illumination. The solar-blind photodetectors have a sharp cutoff around 276 nm. The dark currents of the 40μm diameter devices are measured to be lower than 8 fA for bias voltages up to 20 V. The responsivity of the photodetectors is 0.13 A/W at 272 nm under 20 V reverse bias. The thermally limited detectivity is calculated as $D^*=1.4 \times 10^{14}$ cm $Hz^{1/2}$ W^{-1} for a 40 micron diameter device.

BIBLIOGRAPHY

[1] A. Osinsky, S. Gangopadhyay, B. W. Lim, M. Z. Anwar, M. A. Khan, D. V. Kuksenkov, and H. Temkin, "High UV/visible contrast photodiodes based on epitaxial lateral overgrown GaN layers," Appl. Phys. Lett. **72**, 742 (1998).

[2] T. Tut, N. Biyikli, I. Kimukin, T. Kartaloglu, O. Aytur, M. S. Unlu, and E. Ozbay, "High Bandwidth-Efficiency Solar-Blind AlGaN Schottky Photodiodes with Low Dark Current," Solid-State Electron. **49**, 117 (2005).

[3] U. Chowdhury, M. M. Wong, C. J. Collins, B. Yang, J. C. Denyszyn, J. C. Campbell, and D. Dupuis, "High-performance solar-blind photodetector using an $Al_{0.6}Ga_{0.4}N$ n-type window layer," J. Cryst. Growth **248**, 552 (2003).

[4] N. Biyikli, I. Kimukin, O. Aytur, E. Ozbay, "Solar-blind AlGaN-based p-i-n photodiodes with low dark current and high detectivity", IEEE Photon. Technol. Lett. **16**, 1718 (2004).

[5] T. Li, D. J. H. Lambert, A. L. Beck, C. J. Collins, B. Yang, J. M. M. Wong, U. Chowdhury, R.D. Dupuis and J. C. Campbell**, "**Solar-blind $Al_xGa_{1-x}N$-based metal-semiconductor-metal ultraviolet photodetectors**,"** Electron. Lett. **36**, 1581 (2000).

[6] Razeghi M., Rogalski A., "Semiconductor ultraviolet detectors," J Appl Phys **79**, 7433 (1996).

[7] J. C. Campbell, S. Demiguel, F. Ma, A. Beck, X. Guo, S. Wang, X. Zheng, X. Li, J. D. Beck, M. A. Kinch, A. Huntington, L. A. Coldren, J. Decobert, and N. Tscherptner, **"**Recent advances in avalanche photodiodes **,"** IEEE J. Quantum Electron. **10**, 777 (2004).

[8] Collins C. J., Chowdhury U., Wong M. M., Yang B., Beck A. L., Dupuis R. D., et al., “Improved solar-blind detectivity using an $Al_xGa_{1-x}N$ heterojunction *p–i–n* photodiode,” Appl Phys Lett **80**, 3754 (2002).

[9] Li T., Lambert D. J. H., Wong M. M., Collins C. J., Yang B., Beck A. L., et al**.,** **“**Low-noise back-illuminated $Al_xGa_{1-x}N$-based p-i-n solar-blind ultraviolet photodetectors,” IEEE J Quant Electron **37**,538 (2001).

[10] Y. Wang, K. Brennan, and P. Ruden**,** **“**Theoretical study of a potential ultraviolet avalanching detector based on impact ionization out of confined quantum states **,”** IEEE J. Quantum Electron. **27**, 232 (1991).

[11] P. Ruden and S. Krishnankutty**,** **“**A solar blind, hybrid III-nitride/silicon, ultraviolet avalanche photodiode **,”** IEEE Trans. Electron Devices **46**, 2348 (1999).

[12] C. Sevik and C. Bulutay, “Gain and temporal response of AlGaN solar-blind avalanche photodiodes: an Ensemble Monte Carlo Analysis,” Appl. Phys. Lett. **83**, 1382 (2003).

[13] K. A. McIntosh, R. J. Molnar, L. J. Mahoney, A. Lightfoot, M. W. Geis, K. M. Molvar, I. Melngailis, R. L. Aggarwal, W. D. Goodhue, S. S. Choi, D. L. Spears, and S. Verghese, “GaN avalanche photodiodes grown by hydride vapor-phase epitaxy ,” Appl. Phys. Lett. **75**, 3485 (1999).

[14] J. C. Carrano, D. J. H. Lambert, C. J. Eiting, C. J. Collins, T. Li, S. Wang, B. Yang, A. L. Beck, R. D. Dupuis, and J. C. Campbell, “GaN avalanche photodiodes ,” Appl. Phys. Lett. **76**, 924 (2000).

[15] A. Osinsky, M. S. Shur, R. Gaska, and Q. Chen**,** **“**Avalanche breakdown and breakdown luminescence in p-π-n GaN diodes **,”** Electron. Lett. **34**, 691 (1998).

[16] S. Verghese, K. A. McIntosh, R. J. Molnar, L. J. Mahoney, R. L. Aggarwal, M. W. Geis, K. M. Molvar, E. K. Duerr, and I. Melngailis, **“**GaN avalanche photodiodes operating in linear-gain mode and Geiger mode,” IEEE Electron Device Lett. **48**, 502 (2001).

[17] K. A. McIntosh, R. J. Molnar, L. J. Mahoney, K. M. Molvar, N. Efremov, and S. Verghese, "Ultraviolet photon counting with GaN avalanche photodiodes," Appl. Phys. Lett. **76**, 3938 (2000).

[18] B. Yang, T. Li, K. Heng, C. Collins, S. Wang, J. C. Carrano, R. D. Dupuis, J. C. Campbell, M. J. Schurman, and I. T. Ferguson, **"**Low dark current GaN avalanche photodiodes," IEEE J. Quantum Electron. **36**, 1389 (2000).

[19] J. B. Limb, D. Yoo, J. H. Ryou, W. Lee, S. C. Shen, R. D. Dupuis, M. L. Reed, C. J. Collins, M. Wraback, D. Hanser, E. Preble, N. M. Williams, and K. Evans, "GaN ultraviolet avalanche photodiodes with optical gain greater than 1000 grown on GaN substrates by metal-organic chemical vapor deposition," Appl. Phys. Lett. **89**, 011112 (2006).

[20] T. Tut, M. Gokkavas, B. Butun, S. Butun, E. Ulker, and E. Ozbay, "Experimental evaluation of impact ionization coefficients in $Al_xGa_{1-x}N$ based avalanche photodiodes," Appl. Phys. Lett. **89**, 183524 (2006).

[21] R. McClintock, A. Yasan, K. Minder, P. Kung, and M. Razeghi, "Avalanche multiplication in AlGaN based solar-blind photodetectors," Appl. Phys. Lett. **87**, 241123 (2005)

[22] N. Biyikli, I. Kimukin, T. Tut, O. Aytur, and E. Ozbay, "Solar-blind AlGaN-based Schottky photodiodes with low noise and high detectivity", Appl. Phys. Lett. **81**, 3272 (2002).

[23] Bahaa E. A. Saleh, Malvin C. Teich "Fundamentals of Photonics" John Wiley and Sons, (1991), New Jersey.

[24] Wang S. Y., Bloom D. M., "100 GHz bandwidth planar GaAs Schottky photodiode," Electron Lett **19,** 554 **(**1983).

[25] Ozbay E., Li K. D., Bloom D. M., " 2.0 psec, 150 GHz GaAs Monolithic Photodiode and All-Electronic Sampler," IEEE Photon Technol Lett **3,** 570 **(**1991).

[26] Ozbay E., Islam M. S., Onat B. M., Gokkavas M, Aytur O., Tuttle G., "High-Speed Resonant Cavity Enhanced Schottky Photodiodes," IEEE Photon Technol Lett **9,** 672 **(**1997).

[27] Osinsky A, Gangopadhyay S, Lim B. W., Anwar M. Z., Khan M. A., Kuksenkov D. V., et al. , “Schottky barrier photodetectors based on AlGaN ,” Appl Phys Lett **72,** 742 **(**1998).

[28] Monroy E, Calle F, Pau J. L., Sanchez F. J., Munoz E., Omnes F., et al., “Analysis and modeling of $Al_xGa_{1-x}N$-based Schottky barrier photodiodes,” J Appl Phys **88,** 2081(2000).

[29] Rumyantsev S. L., Pala N., Shur M. S., Gaska R, Levinshtein M. E., Adivarahan V., et al., “Low-frequency noise in $Al_{0.4}Ga_{0.6}N$-based Schottky barrier photodetectors,” Appl Phys Lett **79,** 866 (2001).

[30] Biyikli N., Aytur O., Kimukin I., Tut T., Ozbay E., “Solar-blind AlGaN-based Schottky photodiodes with low noise and high detectivity,” Appl Phys Lett **81,** 3272. **(**2002).

[31] Biyikli N., Kimukin I., Kartaloglu T., Aytur O., Ozbay E., “ High-speed solar-blind photodetectors with indium-thin-oxide Schottky contacts,” Appl Phys Lett **82,** 2344 **(**2003).

[32] Donati S. Prentice Hall, Upper Saddle River, NJ, (2000).

[33] Collins C. J., Li T., Lambert D. J. H., Wong M. M., Dupuis R. D., Campbell J. C., “Selective regrowth of $Al_{0.30}Ga_{0.70}N$ *p–i–n* photodiodes,” Appl Phys Lett **77**,2810 **(**2000).

[34] Gelmont B., Kim K. H., Shur M., “Monte Carlo simulation of electron transport in gallium nitride,” J Appl Phys **74,**1818 **(**1993).

[35] Kolnik J., Oguzman I. H., Brennan K. F., Wang R., Ruden P. P., Wang Y., “Electronic transport studies of bulk zincblende and wurtzite phases of GaN based on an ensemble Monte Carlo calculation including a full zone band structure ,” J Appl Phys **78** , 1033 (1995).

[36] Oguzman I. H., Kolnik J., Brennan K. F., Wang R., Fang T., Ruden P. P., “Hole transport properties of bulk zinc-blende and wurtzite phases of GaN based on an ensemble Monte Carlo calculation including a full zone band structure,” J Appl Phys **80,** 4429 (1996).

[37] Li T., Lambert D. J. H., Wong M. M., Collins C. J., Yang B., Beck A. L., **“**Low-noise back-illuminated $Al_xGa_{1-x}N$-based p-i-n solar-blind ultraviolet photodetectors,” IEEE J Quant Electron **37**, 538 (2001).

[38] W. Yang, T. Nohova, S. Krishnankutty, R. Torreano, S. McPherson, and H. Marsh, “Back-illuminated GaN/AlGaN heterojunction photodiodes with high quantum efficiency and low noise,” Appl. Phys. Lett. **73**, 1086 (1998).

[39] J. C. Carrano, T. Li, D. L. Brown, P. A. Grudowski, C. J. Eiting, R. D. Dupuis, and J. C. Campbell, **“**High-speed pin ultraviolet photodetectors fabricated on GaN **,”** Electron. Lett. **34**, 1779 (1998).

[40] H. Yu, M. K. Ozturk, S. Ozcelik, and E. Ozbay, “Optimization of semi-insulating GaN grown on an AlN/sapphire template by metalorganic chemical vapor deposition,” J. Cryst. Growth **293**, 273 (2006).

[41] H. Yu, W. Strupinski, S. Butun, and E. Ozbay, “Mg-doped AlGaN grown on an AlN/sapphire template by metalorganic chemical vapour deposition ,” Phys. Status Solidi A **203**, 868 (2006).

[42] B. Butun, N. Biyikli, I. Kimukin, O. Aytur, and E. Ozbay, “High-speed 1.55 mm operation of low-temperature-grown GaAs-based resonant-cavity-enhanced p– i– n photodiodes,” Appl. Phys. Lett. **84**, 4185 (2004).

[43] A. Osinsky, S. Gangopadhyay, B. W. Lim, M. Z. Anwar, M. A. Khan, D. V. Kuksenkov, and H. Temkin, “Schottky barrier photodetectors based on AlGaN,” Appl. Phys. Lett. **72**, 742 (1998).

[44] T. Tut, N. Biyikli, I. Kimukin, T. Kartaloglu, O. Aytur, M. S. Unlu, and E. Ozbay, “"High Bandwidth-Efficiency Solar-Blind AlGaN Schottky Photodiodes with Low Dark Current,” Solid-State Electron. **49**, 117 (2005).

[45] U. Chowdhury, M. M. Wong, C. J. Collins, B. Yang, J. C. Denyszyn, J. C. Campbell, and D. Dupuis, “High-performance solar-blind photodetector using an Al0.6Ga0.4N n-type window layer ,” J. Cryst. Growth **248**, 552 (2003).

[46] N. Biyikli, I. Kimukin, O. Aytur, E. Ozbay, “Solar-blind AlGaN-based p-i-n photodiodes with low dark current and high detectivity,” IEEE Photon. Technol. Lett. **16**, 1718 (2004).

[47] T. Li, D. J. H. Lambert, A. L. Beck, C. J. Collins, B. Yang, J. M. M. Wong, U. Chowdhury, R.D. Dupuis and J. C. Campbell**, "**Solar-blind $Al_xGa_{1-x}N$-based metal-semiconductor-metal ultraviolet photodetectors**,"** Electron. Lett. **36**, 1581 (2000).

[48] K. A. McIntosh, R. J. Molnar, L. J. Mahoney, A. Lightfoot, M. W. Geis, K. M. Molvar, I. Melngailis, R. L. Aggarwal, W. D. Goodhue, S. S. Choi, D.L. Spears, and S. Verghese, "GaN avalanche photodiodes grown by hydride vapor-phase epitaxy ," Appl. Phys. Lett. **75**, 3485 (1999).

[49] J. C. Carrano, D. J. H. Lambert, C. J. Eiting, C. J. Collins, T. Li, S. Wang, B. Yang, A. L. Beck, R. D. Dupuis, and J. C. Campbell, "GaN avalanche photodiodes ," Appl. Phys. Lett. **76**, 924 (2000).

[50] A. Osinsky, M. S. Shur, R. Gaska, and, Q. Chen**, "**Avalanche breakdown and breakdown luminescence in p-π-n GaN diodes **,"** Electron. Lett. **34**, 691 (1998).

[51] S. Verghese, K. A. McIntosh, R. J. Molnar, L. J. Mahoney, R. L. Aggarwal, M. W. Geis, K. M. Molvar, E. K. Duerr, and I. Melngailis, **"**GaN avalanche photodiodes operating in linear-gain mode and Geiger mode," IEEE Electron Device Lett. **48**, 502 (2001).

[52] K. A. McIntosh, R. J. Molnar, L. J. Mahoney, K. M. Molvar, N. Efremov, and S. Verghese,"Ultraviolet photon counting with GaN avalanche photodiodes," Appl. Phys. Lett. **76**, 3938 (2000).

[53] B. Yang, T. Li, K. Heng, C. Collins, S. Wang, J. C. Carrano, R. D. Dupuis, J. C. Campbell, M. J. Schurman, and I. T. Ferguson, **"**Low dark current GaN avalanche photodiodes," IEEE J. Quantum Electron. **36**, 1389 (2000).

[54] T. Tut, N. Biyikli, I. Kimukin, T. Kartaloglu, O. Aytur, M. S. Unlu, and E. Ozbay, "High Bandwidth-Efficiency Solar-Blind AlGaN Schottky Photodiodes with Low Dark Current," Solid-State Electron. **49**, 117 (2005).

[55] Ismail H. Oguzman, Enrico Bellotti, Kevin F. Brennan, Jan Kolnik, Rongping Wang, and P. Paul Ruden, "Theory of hole initiated impact ionization in bulk zincblende and wurtzite GaN ," J. Appl. Phys. **81**, 7827 (1997).

[56] J. C. Cao and X. L. Lei**,** **“**Nonparabolic multivalley balance-equation approach to impact ionization: Application to wurtzite GaN ,” Eur. Phys. J. B **7**, 79 (1999).

[57] C. Bulutay, “Electron initiated impact ionization in AlGaN alloys," Semicond. Sci. Technol. **17**, L59 (2002).

[58] K. Kunihiro, K. Kasahara, Y. Takahashi, and Y. Ohno, **“**Experimental evaluation of impact ionization coefficients in GaN,” IEEE Electron Device Lett. **20**, 608 (1999).

[59] M. H. Woods, W. C. Johnson, and M. A. Lampert, Solid-State Electron. **16**, 381 (1972).

[60] N. Tabatabaie, V. M. Robbins, N. Pan, and G. E. Stillman, “ Impact ionization coefficients in (111) InP,” Appl. Phys. Lett. **46**, 182 (1985).

[61] S. L. Fu, T. P. Chin, M. C. Ho, C. W. Tu, and P. M. Asbeck, “Impact ionization coefficients in (100) GaInP **, ”**Appl. Phys. Lett. **66**, 3507 (1995).

[62] B. K. Ng, J. P. David, S. A. Plimmer, M. Hopkinson, R. C. Tozer, and G. J. Rees, **“**Impact ionization coefficients of Al0.8Ga0.2As,” Appl. Phys. Lett. **77**, 4374 (2000).

[63] C. Bulutay, “Electron initiated impact ionization in AlGaN alloys”, Semicond. Sci. Technol. **17**, L59 (2002).

[64] E. Ozbay, N. Biyikli, I. Kimukin, T. Tut, T. Kartaloglu, and O. Aytur, “High-Performance Solar-Blind Photodetectors Based on $Al_xGa_{1-x}N$ Heterostructures,” IEEE J. Sel. Top. Quantum Electron. **10**, 742 (2004).

[65] C. J. Collins, U. Chowdhury, M. M. Wong, B. Yang, A. L. Beck, and R. D. Dupuis, “Improved solar-blind external quantum efficiency of back-illuminated $Al_xGa_{1-x}N$ heterojunction pin photodiodes,” Electron. Lett. **38**, 824 (2002).

[66] N. Biyikli, T. Kartaloglu, O. Aytur, I. Kimukin, and E. Ozbay, “High-speed visible blind GaN-based indium tin oxide Schottky photodiodes,” Appl. Phys. Lett. **79**, 2838 (2001).

[67] N. Biyikli, I. Kimukin, T. Tut, O. Aytur, and E. Ozbay, “Solar-blind AlGaN-based Schottky photodiodes with low noise and high detectivity,” Appl. Phys. Lett. **81**, 3272 (2002).

[68] S. Butun, M. Gokkavas, HongBo Yu, and E. Ozbay, “Low dark current metal-semiconductor-metal photodiodes based on semi-insulating GaN,” Appl. Phys. Lett. **89**, 073503 (2006).

[69] J. C. Campbell, S. Demiguel, F. Ma, A. Beck, X. Guo, S. Wang, X. Zheng, X. Li, J. D. Beck, M. A. Kinch, A. Huntington, L. A. Coldren, J. Decobert, and N. Tscherptner, **“**Recent advances in avalanche photodiodes,” IEEE J. Quantum Electron. **10**, 777 (2004).

[70] T. Tut, S. Butun, B. Butun, M. Gokkavas, H. B. Yu, and E. Ozbay,” Solar-blind AlGaN-based avalanche photodiodes,” Appl. Phys. Lett. **87**, 223502 (2005).

[71] N. Biyikli, I. Kimukin, T. Kartaloglu, O. Aytur, and Ekmel Ozbay, “High-speed solar-blind AlGaN-based metal–semiconductor–metal photodetectors,” Phys. Status Solidi C **7**, 2314 (2003).

[72] Y. Wang, K. Brennan, and P. Ruden, **“**Theoretical study of a potential ultraviolet avalanching detector based on impact ionization out of confined quantum states ,” IEEE J. Quantum Electron. **27**, 232 (1991).

[73] P. Ruden and S. Krishnankutty, “A solar blind, hybrid III-nitride/silicon, ultraviolet avalanche photodiode,” IEEE Trans. Electron Devices **46**, 2348 (1999).

[74] C. Sevik and C. Bulutay, “Gain and temporal response of AlGaN solar-blind avalanche photodiodes: an Ensemble Monte Carlo Analysis,” Appl. Phys. Lett. **83**, 1382 (2003).